PATH INTEGRAL DYNAMICS METHODS FOR SIMULATING QUANTUM PROCESSES IN MULTI-ELECTRON, CONDENSED-PHASE SYSTEMS

A Dissertation

Presented to the Faculty of the Graduate School

of Cornell University

in Partial Fulfillment of the Requirements for the Degree of

Doctor of Philosophy

by

Jessica Ryan Duke

May 2017

PATH INTEGRAL DYNAMICS METHODS FOR SIMULATING QUANTUM PROCESSES IN MULTI-ELECTRON, CONDENSED-PHASE SYSTEMS

Jessica Ryan Duke, Ph.D.

Cornell University 2017

Understanding the mechanisms and timescales of charge and energy transfer processes in large, complex molecular systems is an essential step towards the rational design of a wide variety of renewable energy technologies. Unfortunately, the quantum mechanical nature of these reactions, where nuclear motions mediate transitions between electronic states, makes them infeasible to simulate exactly in many-body systems because of the scaling limitations of exact quantum dynamics methods. Developing approximate quantum dynamics methods capable of efficiently, yet accurately describing quantum processes in high-dimensional systems is, therefore, an ongoing effort in the field of theoretical chemistry and the focus of this dissertation.

The two methods we discuss here are based on the imaginary-time path integral formulation of the quantum Boltzmann distribution that allows quantum degrees of freedom to be represented by classical "ring polymers" in an extended phase space [1]. Specifically, these methods are versions of the promising ring polymer molecular dynamics (RPMD) method for approximating quantum real-time thermal correlation functions using classical ring polymer trajectories [2, 3]. The first method we discuss, mean field (MF)-RPMD, extends the original RPMD formulation to multi-electron systems and describes nuclear dynamics on an average potential energy surface [4]. We show how a novel implementation of this method for rate calculations yields accurate electron transfer rate

constants across a wide range of parameter regimes [5].

The second method we describe, mapping variable (MV)-RPMD, captures electronic state transitions using only classical MD trajectories by employing an exact mapping from discrete electronic states to classical phase-space variables [6]. In order to use this method to study photochemistry, we derive a function in the MV-RPMD framework that reports on electronic state populations as a function of time, and we introduce a constraint protocol to initialize an MV-RPMD simulation to a particular electronic state. We numerically demonstrate the accuracy of this population function and constraint technique in the context of model systems undergoing electronic state transmission/reflection and photodissociation [7].

BIOGRAPHICAL SKETCH

Native to Birmingham, AL, Jess nurtured her interest in science and mathematics at the Jefferson County International Baccalaureate high school. For her undergraduate studies, she accepted full scholarship to The University of Alabama, where she majored in chemistry and mathematics and minored in the Computer-Based Honors Program. After developing a strong interest in research through enriching internships in breast cancer drug discovery, shrimp aquaculture, and carbon sequestration, she made the bold move to frigid Ithaca, NY to pursue her doctoral degree at Cornell University in her primary area of interest, chemical physics. As a National Science Foundation Graduate Research Fellow at Cornell, she has spent her time developing mathematical methods for simulating reactions important for renewable energy harvesting. In her spare time, Jess enjoys reading fantasy novels and WWII nonfiction, training her puppy to perform amusing tricks, and playing sports (which these days gets translated as "going to physical therapy").

For my mom: since you didn't get a chance to attend college, I went long enough for both of us.

ACKNOWLEDGEMENTS

Completion of this thesis would not have been possible without the unwavering support of my family, friends, and academic advisors. Here I acknowledge these wonderful individuals.

First, to my mom, thank you for always reassuring me that "it's never too late to turn the car around and drive back to Alabama" and for being my sturdiest pillar of support. To my dad, thank you for helping me keep my priorities straight when times got stressful; in other words, "Roll Tide." Harry, thank you for your service to our country and for being the ultimate inspiration for my career choice. And Nana and Papa, thank you for loving me even though I chose to move so far away from home. I have missed all of you terribly over the past 5 years, but in many ways that has made our visits even more special.

During my time at Cornell, I have had the pleasure of working closely with an intelligent and entertaining research group as well as with some of the greatest mentors imaginable. Thank you Nandini for having the patience and brilliance to answer my unending questions and the kindness to allow me to spend extra time pursuing my dreams. Thank you Professor Ezra for sharing your wisdom in all things related to research, careers, and knee surgery. And thank you Professors Loring and Marohn for guiding me along my academic journey.

I also consider myself extremely lucky to have made incredible life-long friends at Cornell. In particular, I thank Kyle and Molly, my closest friends and fellow vacationers, for making these past few years extremely fun. As for my best furry friend, I thank Toast for encouraging me to finish this thesis by making sure I did not spend too much time sleeping. And last but certainly not least, thank you Dave for simply being the best in every way.

The work described in this dissertation was funded by a National Science Foundation Graduate Research Fellowship (grant no. DGE-1144153), a startup grant from Cornell University, a National Science Foundation CAREER grant (award no. CHE-1555205), and a Sloan Foundation Fellowship. Parts of Chapter 3 were reproduced from Ref. 5 with permission from the authors. Parts of Chapter 4 and Appendix B were reproduced from Ref. 7, also with permission from the authors.

TABLE OF CONTENTS

LIST OF TABLES

LIST OF FIGURES

LIST OF ABBREVIATIONS

COM	Center of Mass
DVR	Discrete Variable Representation
ET	Electron Transfer
FGR	Fermi's Golden Rule
KC-RPMD	Kinetically Constrained Ring Polymer Molecular Dynamics
KT	Kramers Theory
LSC-IVR	Linearized Semiclassical Initial Value Representation
MC	Monte Carlo
MD	Molecular Dynamics
MF-RPMD	Mean Field Ring Polymer Molecular Dynamics
MMST	Meyer-Miller-Stock-Thoss
MT	Marcus Theory
MV-RPMD	Mapping Variable Ring Polymer Molecular Dynamics
PI	Path Integral
PIMC	Path Integral Monte Carlo
PIMD	Path Integral Molecular Dynamics
RPMD	Ring Polymer Molecular Dynamics
SEO	Singly Excited Oscillator
TS	Transition State
TST	Transition State Theory
ZPE	Zero Point Energy

CHAPTER 1

INTRODUCTION

From enzymatic activity to renewable energy harvesting, a remarkable number of important reaction pathways in condensed-phase systems are driven by quantum mechanical charge and energy transfer processes [8–17]. By understanding the mechanisms of these processes—as well as the physical and chemical motifs that make them possible—we make progress towards rationally designing improved technologies based on them, including artificial photosynthesis devices, molecular electronics, and organic photovoltaics. However, studying these reactions has not proven simple, as many standard theoretical and experimental approaches fail to provide sufficient information. Statistical calculations help elucidate energy landscapes but cannot conclusively determine dynamical pathways in complex systems. And while time-resolved experiments offer insight into long-time behavior, they struggle to probe crucial sub-femtosecond dynamics common to these reactions.

In theory, real-time dynamics simulations offer an attractive alternative: they allow for complete control over reaction conditions, provide detailed atomistic pictures of reactive events, and can probe the sub-femtosecond dynamics that experiments cannot easily access. Unfortunately, dynamics simulations present certain complications of their own. The quantum mechanical nature of these charge and energy transfer reactions makes them infeasible to study exactly in large systems because of the scaling limitations of exact quantum dynamics methods [18]. On the other hand, many of the more efficient classical molecular dynamics (MD) approaches fail to capture important quantum effects. With this in mind, numerous approximate quantum dynamics methods have been devel-

oped over the past few decades [2, 3, 6, 19–30], many of which are still unsuitable for condensed-phase problems that necessitate efficiency and preservation of a thermal distribution. The most accurate semiclassical methods, for instance, remain impractical for large systems [22], whereas more efficient versions fail to preserve detailed balance [21, 28]. Mixed quantum-classical methods likewise do not generally conserve thermal distributions and also suffer from uncontrolled approximations that result from interfacing quantum and classical dynamics [23, 30]. Among the more promising approaches, however, is a class of methods based on imaginary-time path integrals (PIs) that employ classical trajectories to capture quantum dynamics effects, while also conserving the Boltzmann distribution [2, 3, 20].

One PI method in particular, ring polymer molecular dynamics (RPMD), has emerged as an accurate and efficient technique for the direct dynamic simulation of thermal charge and energy transfer processes in the condensed phase [2, 3]. By exclusively employing classical trajectories for the dynamics, RPMD not only scales almost linearly with system size but also describes all degrees of freedom within a uniform dynamic framework and thus does not suffer from the interfacing problems associated with mixed quantum-classical methods. This method has been successfully employed to calculate accurate self-diffusion coefficients for liquid parahydrogen [31], hydride transfer rates in enzymes [32], and electron transfer rates between transition metal complexes in solution [33], among a variety of other applications [34–47]. One disadvantage of the original RPMD formulation, however, is that it represents individual electrons as explicit particles. This choice of representation limits the method's applicability to distinguishable-electron reactions in order to avoid complications associated with accounting for fermionic statistics in multi-electron systems.

The success of RPMD for distinguishable-electron processes provides great incentive for developing versions of the method that are applicable to a broader range of reactions [6, 26, 27]. In this dissertation, we describe our recent progress towards this goal. Specifically, we present two extensions of RPMD for calculating chemical reaction rates and simulating photo-initiated dynamics in multi-electron, multi-state systems. The first extension we will describe is based on an existing version of RPMD called mean field (MF)-RPMD, which avoids the distinguishable-electron problem by representing chemical systems using discrete electronic *states* rather than with explicit electron particles [4]. However, because this method effectively propagates nuclear dynamics on a mean potential energy surface, it has failed to describe processes involving weakly-coupled electronic states in previous applications. In the following sections, we demonstrate a novel implementation of MF-RPMD that allows us to accurately calculate reaction rate constants across the full range of electronic coupling strengths [5]. The second extension we will describe, mapping variable (MV)-RPMD, originated in our research group and overcomes the disadvantages of MF-RPMD by employing *continuous* electronic state variables that can be used in classical MD simulations [6]. We demonstrate how these variables may be constrained in order to initialize a simulation to a specific state as well as how they can be used to track transitions to other states over the course of a simulation—together these advances allow us to use MV-RPMD to model photo-initiated dynamics [7].

This dissertation is organized as follows: we begin by reviewing the original RPMD formulation and discuss its advantages and disadvantages in more detail. In Chapter 3, we introduce MF-RPMD and describe our novel way of using it to calculate accurate reaction rate constants across a wide range of parameter

regimes. Chapter 4 focuses on MV-RPMD and how it is used to simulate photochemical dynamics. Finally, in Chapter 5, we summarize our progress and discuss future directions of this research.

CHAPTER 2

REVIEW OF RING POLYMER MOLECULAR DYNAMICS

Before considering extensions of RPMD, it is helpful to review the original method in order to fully appreciate the theory, its advantages, and its limitations. As we will see, the basic idea is to circumvent the scaling problems of quantum dynamics by representing quantum systems using classical frameworks. In this chapter, we will first review how we can use classical mechanics to generate quantum statistics and then build off that idea to tackle quantum dynamics problems using efficient classical MD algorithms. This formulation leads to a convenient and accurate approach particularly for calculating rate constants.

2.1 The Classical Isomorphism

Directly solving equations that describe the quantum mechanical statistics of large, complex molecular systems remains a challenge. Fortunately, it has been known for many years that an isomorphism exists between the equilibrium distribution of a quantum system and that of a fictitious classical system in extended phase space [1]. To see this, consider the canonical partition function, Z, of a quantum mechanical system at inverse temperature $\beta = 1/k_B T$:

$$Z = \mathrm{Tr}\left[e^{-\beta\hat{H}}\right] = \mathrm{Tr}\left[e^{-\beta(\hat{K}+\hat{V})}\right], \tag{2.1}$$

where the Hamiltonian $\hat{H}$ is the sum of the kinetic and potential energy operators, $\hat{K}$ and $\hat{V}$ respectively, which in general do not commute. To more easily calculate the exponential in the equation above, we make use of the Trotter the-

orem [48],

$$e^{-\beta(\hat{K}+\hat{V})} = \lim_{N\to\infty}\left(e^{-\frac{\beta}{2N}\hat{V}}e^{-\frac{\beta}{N}\hat{K}}e^{-\frac{\beta}{2N}\hat{V}}\right)^N, \tag{2.2}$$

which allows us to separately evaluate kinetic and potential energy terms. Substituting the Trotter theorem into Eq. (2.1) yields

$$Z = \lim_{N\to\infty}\mathrm{Tr}\left[\left(e^{-\frac{\beta}{2N}\hat{V}}e^{-\frac{\beta}{N}\hat{K}}e^{-\frac{\beta}{2N}\hat{V}}\right)^N\right] = \lim_{N\to\infty}\mathrm{Tr}\left[\left(e^{-\frac{\beta}{N}\hat{V}}e^{-\frac{\beta}{N}\hat{K}}\right)^N\right], \tag{2.3}$$

where the second equality results from the cyclic permutability of the trace.

For a system occupying a single potential energy surface described by a Hamiltonian of the form $\hat{H} = \frac{\hat{\mathbf{P}}^2}{2M} + V\left(\hat{\mathbf{R}}\right)$, we evaluate the trace in position-space. Additionally, we insert $N-1$ copies of the position-space identity operator, $\hat{\mathbb{1}} = \int d\mathbf{R}\ |\mathbf{R}\rangle\langle\mathbf{R}|$, between each $e^{-\frac{\beta}{N}\hat{V}}e^{-\frac{\beta}{N}\hat{K}}$ term:

$$Z = \lim_{N\to\infty}\int d\mathbf{R}_1\cdots\int d\mathbf{R}_N\ \langle\mathbf{R}_1|e^{-\frac{\beta}{N}\hat{V}}e^{-\frac{\beta}{N}\hat{K}}|\mathbf{R}_2\rangle\cdots\langle\mathbf{R}_N|e^{-\frac{\beta}{N}\hat{V}}e^{-\frac{\beta}{N}\hat{K}}|\mathbf{R}_1\rangle. \tag{2.4}$$

(Here and throughout, bold font denotes multi-dimensional vectors.) Further, since the potential energy operator is diagonal in the coordinate representation, we obtain

$$Z = \lim_{N\to\infty}\int\{d\mathbf{R}_\alpha\}\prod_{\alpha=1}^{N}e^{-\frac{\beta}{N}V(\mathbf{R}_\alpha)}\langle\mathbf{R}_\alpha|e^{-\frac{\beta}{N}\hat{K}}|\mathbf{R}_{\alpha+1}\rangle. \tag{2.5}$$

In Eq. (2.5), the notation $\int\{d\mathbf{R}_\alpha\}$ represents integration over all $\mathbf{R}_\alpha$ variables, and the trace requires that $\mathbf{R}_{N+1} = \mathbf{R}_1$.

To evaluate the kinetic energy matrix elements, we insert additional copies of identity in the momentum representation, $\hat{\mathbb{1}} = \int d\mathbf{P}\ |\mathbf{P}\rangle\langle\mathbf{P}|$. Noting that $\hat{K}|\mathbf{P}\rangle = \frac{\mathbf{P}\cdot\mathbf{P}}{2M}|\mathbf{P}\rangle$ and that the inner product between position and momentum eigenstates for a d-dimensional system is given by

$$\langle\mathbf{R}|\mathbf{P}\rangle = \left(\frac{1}{2\pi\hbar}\right)^{\frac{d}{2}}e^{\frac{i}{\hbar}\mathbf{P}\cdot\mathbf{R}}, \tag{2.6}$$

we find

$$\langle \mathbf{R}_\alpha | e^{-\frac{\beta}{N}\hat{K}} | \mathbf{R}_{\alpha+1} \rangle = \left(\frac{1}{2\pi\hbar} \right)^d \int_{-\infty}^{\infty} d\mathbf{P}\, e^{-\frac{\beta}{N}\frac{\mathbf{P}\cdot\mathbf{P}}{2M} + \frac{i}{\hbar}\mathbf{P}\cdot(\mathbf{R}_\alpha - \mathbf{R}_{\alpha+1})} = \left(\frac{MN}{2\pi\beta\hbar^2} \right)^{\frac{d}{2}} e^{-\frac{MN}{2\beta\hbar^2}(\mathbf{R}_\alpha - \mathbf{R}_{\alpha+1})\cdot(\mathbf{R}_\alpha - \mathbf{R}_{\alpha+1})}, \tag{2.7}$$

where the second equality emerges after completing the square in the exponential and evaluating the resulting Gaussian integral. Substituting Eq. (2.7) into Eq. (2.5) gives

$$Z = \lim_{N\to\infty} \left(\frac{MN}{2\pi\beta\hbar^2} \right)^{\frac{dN}{2}} \int \{d\mathbf{R}_\alpha\} \prod_{\alpha=1}^{N} e^{-\frac{\beta}{N}V(\mathbf{R}_\alpha)} e^{-\frac{MN}{2\beta\hbar^2}(\mathbf{R}_\alpha - \mathbf{R}_{\alpha+1})\cdot(\mathbf{R}_\alpha - \mathbf{R}_{\alpha+1})}. \tag{2.8}$$

The previous expression is immediately recognized as a classical configuration integral describing the position distribution of a system containing d-dimensional "ring polymers"; as formulated, these ring polymers (Fig. 2.1) each contain N classical particles, or "beads," that interact with their nearest neighbors through harmonic spring forces and are subject on average to the external potential $V(\mathbf{R})$ at inverse temperature β. Note that in practice Eq. (2.8) converges for a finite number of beads, with smaller masses usually requiring more beads for convergence. One may also employ a "mixed-time slicing" approach where N can differ for each degree of freedom [49].

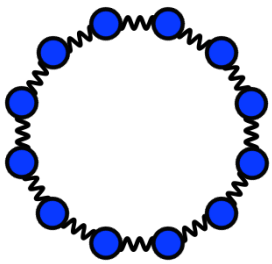

Figure 2.1: A ring polymer.

For simulation purposes, it is also convenient to introduce momentum for each of the beads. This is achieved by multiplying Z above by normalized Gaus-

sian momentum integrals, and in doing so we arrive at an expression for the full partition function of the ring polymer system [50]:

$$Z = \lim_{N\to\infty} \left(\frac{1}{2\pi\hbar}\right)^{dN} \int \{d\mathbf{R}_\alpha\} \int \{d\mathbf{P}_\alpha\}\, e^{-\frac{\beta}{N} H_N(\{\mathbf{R}_\alpha,\mathbf{P}_\alpha\})}, \tag{2.9}$$

where H_N represents the classical ring polymer Hamiltonian,

$$H_N = \sum_{\alpha=1}^{N} \left[\frac{\mathbf{P}_\alpha \cdot \mathbf{P}_\alpha}{2M} + V(\mathbf{R}_\alpha) + \frac{MN^2}{2\beta^2\hbar^2} (\mathbf{R}_\alpha - \mathbf{R}_{\alpha+1}) \cdot (\mathbf{R}_\alpha - \mathbf{R}_{\alpha+1}) \right]. \tag{2.10}$$

As a final note, the same mathematical approach taken above can be used to find classical expressions for thermal quantum expectation values. Consider, for example, the expectation value of a position-dependent operator $\hat{A}$,

$$\langle \hat{A} \rangle = \lim_{N\to\infty} \frac{1}{Z} \left(\frac{1}{2\pi\hbar}\right)^{dN} \int \{d\mathbf{R}_\alpha\} \int \{d\mathbf{P}_\alpha\}\, e^{-\frac{\beta}{N} H_N(\{\mathbf{R}_\alpha,\mathbf{P}_\alpha\})} A_N(\{\mathbf{R}_\alpha\}) \tag{2.11}$$

with

$$A_N(\{\mathbf{R}_\alpha\}) = \frac{1}{N} \sum_{\alpha=1}^{N} A(\mathbf{R}_\alpha). \tag{2.12}$$

This method of expressing the Boltzmann operator as a product of matrix elements is often referred to as "path integral discretization," an idea originally used by Feynman to represent quantum time evolution as a sum over classical paths [51]. (Here we say we work in "imaginary time" because the simple substitution $\beta \to it/\hbar$ leads us back to Feynman's original formulation.) The virtue of this approach is that we have derived Eqs. (2.9) and (2.11) exactly from their quantum mechanical counterparts, and thus they give us an avenue by which to determine the equilibrium properties of quantum systems using classical mechanics. Two popular techniques for solving these equations are path integral Monte Carlo (PIMC) [52], which involves importance sampling phase-space configurations based on the Boltzmann factor $e^{-\frac{\beta}{N} H_N(\{\mathbf{R}_\alpha,\mathbf{P}_\alpha\})}$, and path integral molecular dynamics (PIMD) [50], which samples an equivalent distribution

along a thermostatted classical trajectory obtained by integrating Hamilton's equations of motion,

$$\dot{R}_{j,\alpha} = +\frac{\partial H_N}{\partial P_{j,\alpha}}, \quad \dot{P}_{j,\alpha} = -\frac{\partial H_N}{\partial R_{j,\alpha}}. \tag{2.13}$$

Both of these methods tend to be efficient for systems containing up to hundreds, sometimes thousands, of atoms.

2.2 Ring Polymer Molecular Dynamics

2.2.1 General Theory

In the previous section, we explored exact ways of calculating quantum statistical averages using classical mechanical techniques. While these methods have proven extremely useful for studying time-independent properties of quantum systems, a complete understanding of many charge and energy transfer reactions requires the capability to calculate *dynamical* properties. More specifically, we seek similar classical approaches for calculating quantum time-dependent thermal correlation functions. The standard form of the real-time quantum thermal correlation function is

$$C_{AB}(t) = \frac{1}{Z}\mathrm{Tr}\left[e^{-\beta\hat{H}}\hat{A}e^{+i\hat{H}t/\hbar}\hat{B}e^{-i\hat{H}t/\hbar}\right]. \tag{2.14}$$

Alternatively, one may also consider the Kubo-transformed version [53],

$$\widetilde{C}_{AB}(t) = \frac{1}{\beta Z}\int_0^\beta d\lambda\ \mathrm{Tr}\left[e^{-(\beta-\lambda)\hat{H}}\hat{A}e^{-\lambda\hat{H}}e^{+i\hat{H}t/\hbar}\hat{B}e^{-i\hat{H}t/\hbar}\right], \tag{2.15}$$

which is a more symmetric and thus a more classical construction of the correlation function. The two versions are related through their Fourier transforms,

$$C_{AB}(\omega) = \frac{\beta\hbar\omega}{1-e^{-\beta\hbar\omega}}\widetilde{C}_{AB}(\omega), \tag{2.16}$$

so knowledge of one is sufficient to determine the other.

Rigorous path integral discretization of Eq. (2.14) or (2.15) (i.e. Feynman's formulation) leads to a variety of exact and approximate quantum dynamics methods [22, 54, 55]. Unless further approximations are made, however, many of these methods remain too computationally demanding to be useful for studying large systems. The philosophy behind ring polymer molecular dynamics [2, 3] differs slightly: we saw in Section 2.1 that a classical representation of the quantum equilibrium expectation value is given by Eq. (2.11). Using the same discretization approach, one can show that the Kubo-transformed correlation function at time zero has a similar classical analogue [2]:

$$\widetilde{C}_{AB}(0) = \lim_{N\to\infty} \frac{1}{Z}\left(\frac{1}{2\pi\hbar}\right)^{dN} \int \{d\mathbf{R}_\alpha\} \int \{d\mathbf{P}_\alpha\}\, e^{-\frac{\beta}{N}H_N} A_N(0) B_N(0), \tag{2.17}$$

where again

$$A_N = \frac{1}{N}\sum_{\alpha=1}^{N} A(\mathbf{R}_\alpha), \quad B_N = \frac{1}{N}\sum_{\alpha=1}^{N} B(\mathbf{R}_\alpha), \tag{2.18}$$

and H_N refers to the classical ring polymer Hamiltonian in Eq. (2.10). RPMD postulates that Eq. (2.17) also holds for $t > 0$ such that [2]

$$\widetilde{C}_{AB}(t) \approx \lim_{N\to\infty} \frac{1}{Z}\left(\frac{1}{2\pi\hbar}\right)^{dN} \int \{d\mathbf{R}_\alpha\} \int \{d\mathbf{P}_\alpha\}\, e^{-\frac{\beta}{N}H_N} A_N(0) B_N(t). \tag{2.19}$$

Although a mathematical route from the quantum Kubo-transformed time correlation function to Eq. (2.19) has been established [56, 57], a detailed understanding of the physical nature of the approximation remains elusive. Nonetheless, in practice RPMD has been shown to work quite well for many condensed-phase problems, particularly at short times [32–47]. Evaluating the integral in Eq. (2.19) involves first generating an initial distribution of ring polymer configurations using either PIMC or PIMD. An ensemble of ring polymer MD trajec-

tories is then launched from this distribution and propagated according to the Hamiltonian H_N, with dynamical properties averaged over the ensemble.

2.2.2 Justification and Applicability

Despite the lack of proof for $t > 0$, use of RPMD for approximating quantum dynamics in certain systems is justified for multiple reasons. First, since its inception, others have established quantitative connections between RPMD and quantum rate theory [58, 59] as well as between RPMD and Matsubara dynamics, an accurate yet computationally inefficient method derivable from the exact quantum time-correlation function [56, 57]. Second, it is not too difficult to discern which quantum effects are included in Eq. (2.19) and which are absent, and this knowledge guides our choice of application. The harmonic spring terms in the ring polymer Hamiltonian ensure that, unlike single classical particles, ring polymers conserve zero point energy (ZPE), and the delocalized nature of the ring polymer allows it to capture quantum dispersion as well as tunneling through energy barriers. Notably missing, however, is real-time quantum coherence. For this reason, condensed-phase problems where thermal averaging and strong inter-mode coupling lead to rapid quantum decoherence are ideal target applications for this method.

Further, formulating Eqs. (2.19), (2.11), and (2.9) in coordinate space makes them useful for systems containing distinguishable particles but inaccurate for systems involving indistinguishable bosons or fermions—to describe the latter, one would need to incorporate bosonic and/or fermionic statistics into the equations. The version of RPMD presented above is thus limited to

distinguishable-particle processes. Fortunately, many interesting and important reactions such as electron transfer or proton-coupled electron transfer fall into this category [8, 10].

Lastly, Eq. (2.19) describes systems at thermal equilibrium, and propagating dynamics using the classical Hamiltonian derived from the Boltzmann factor ensures preservation of this distribution in time. Recently, Welsch et al. also showed that nearly all of the important properties of RPMD are retained when describing relaxation dynamics from non-equilibrium initial conditions [60], thereby justifying use of this method for studying vertical excitation processes and for calculating reaction rates.

2.3 Rate Theory

Given the connection between RPMD and quantum rate theory, it is perhaps not surprising that some of the most successful applications of RPMD to date involve the calculation of reaction rate constants. Methods like this that are capable of efficiently calculating reaction rates in many-body systems are extremely useful for understanding how different features of a chemical system influence the speed of a reaction. They can also be used to predict rates in new systems and guide experimentalists towards designing better materials for a variety of applications.

The RPMD reaction rate constant can be written in terms of the flux-side correlation function [61, 62]

$$k = \lim_{t\to\infty} \frac{\left\langle \delta\left(\xi\left(\mathbf{R}_0\right) - \xi^{\ddagger}\right)\dot{\xi}_0\, h\left(\xi\left(\mathbf{R}_t\right) - \xi^{\ddagger}\right)\right\rangle}{\left\langle h\left(\xi^{\ddagger} - \xi\left(\mathbf{R}_0\right)\right)\right\rangle}, \tag{2.20}$$

where angular brackets indicate canonical ensemble averages, h represents the Heaviside function, δ is the Dirac delta function, and the subscript 0 refers to the initial value of the corresponding variable. In Eq. (2.20), the function $\xi(\mathbf{R})$ denotes a general reaction coordinate that distinguishes between reactants and products via the dividing surface defined as $\xi(\mathbf{R}) = \xi^{\ddagger}$. For easier computation, Eq. (2.20) is usually factored into a purely statistical transition state theory (TST) rate estimate, k_{TST}, and a time-dependent coefficient, $\kappa(t)$, that accounts for dynamic recrossing at the dividing surface [63]. One such factoring is

$$\begin{aligned} k &= k_{\mathrm{TST}} \times \lim_{t\to\infty} \kappa(t) \\ &= \frac{\left\langle \dot{\xi}_0 \, h\left(\dot{\xi}_0\right)\right\rangle_c \left\langle \delta\left(\xi\left(\mathbf{R}_0\right) - \xi^{\ddagger}\right)\right\rangle}{\left\langle h\left(\xi^{\ddagger} - \xi\left(\mathbf{R}_0\right)\right)\right\rangle} \times \lim_{t\to\infty} \frac{\left\langle \dot{\xi}_0 \, h\left(\xi\left(\mathbf{R}_t\right) - \xi^{\ddagger}\right)\right\rangle_c}{\left\langle \dot{\xi}_0 \, h\left(\dot{\xi}_0\right)\right\rangle_c \left\langle \delta\left(\xi\left(\mathbf{R}_0\right) - \xi^{\ddagger}\right)\right\rangle}, \end{aligned} \tag{2.21}$$

where $\langle \cdots \rangle_c$ indicates an ensemble average with the system constrained to the transition state (TS).

The first term on the righthand side of Eq. (2.21), k_{TST}, represents the average positive velocity of the reaction coordinate at the transition state barrier multiplied by the probability of the system reaching the transition state from the reactant state. This term does not involve dynamical properties and thus can be calculated using either PIMC or PIMD. The second term on the righthand side of Eq. (2.21), $\kappa(t)$, represents the fraction of trajectories that form product after reaching the transition state and, therefore, does involve dynamical properties. This term is obtained by initializing RPMD trajectories to the transition state and calculating the correlation between initial forward flux and final position on the product side of the dividing surface.

Since Craig and Manolopoulos introduced RPMD rate theory in 2005 [34, 35], they and others have shown it works well for a variety of systems. Boekelheide et al., for example, applied the theory to compare the influence of local and long-

range protein motions on the rate of hydride transfer in the enzyme *Escherichia coli* dihydrofolate reductase, disproving the popular notion that nonlocal vibrational dynamics play an important role in its catalytic activity [32]. More recently, Kenion and Ananth used RPMD to study the rate of electron transfer between transition metal complexes in solution and helped clarify the contribution of outer sphere (i.e. solvent) reorganization in driving the reaction [33]. However, one must exercise caution when applying the method, as Menzeleev et al. found that it severely overestimates rates for rare cases where the Gibbs free energy of activation is negative and its absolute magnitude exceeds that of the solvent reorganization energy (i.e. the Marcus "inverted regime") [42].

2.4 Summary

In this chapter, we reviewed the isomorphism between quantum and classical ring polymer systems at equilibrium, and we explored the basic theory behind ring polymer molecular dynamics, an efficient yet approximate quantum dynamics method that preserves the thermal distribution and provides a consistent dynamic framework for reactions. We also discussed in more detail one of RPMD's most successful applications, reaction rate calculation. However, notable shortcomings of this method include its failure to capture real-time coherence effects and its treatment of electrons (and protons) as distinguishable particles.

Given RPMD's efficiency, its demonstrated success for certain condensed-phase problems, and its advantages over other approaches, we seek versions of the method that are applicable to a broader class of systems. In this dissertation,

we specifically address the distinguishable-electron problem by developing versions of RPMD in state space that are applicable to multi-electron reactions.

CHAPTER 3

REACTION RATES FROM MEAN FIELD RING POLYMER MOLECULAR DYNAMICS

In the previous chapter, we emphasized one significant drawback of the ring polymer molecular dynamics method, its limitation to distinguishable-particle reactions. While a method like this can still be useful for studying a variety of processes, including single electron transfer, many important reactions involve the dynamics of multiple electrons. In this chapter, we discuss a version of RPMD, mean field RPMD [4], that is formulated for multi-electron systems, and we describe a novel implementation of this method for calculating nonadiabatic reaction rate constants [5].

3.1 State Space Path Integral Discretization

Perhaps the simplest way to overcome the distinguishable electron problem is to avoid the position-space representation altogether. We wish instead to formulate RPMD in state space, where we represent the distinct multi-electron configurations of a chemical system using a set of diabatic potential energy curves, expressed as functions of nuclear coordinates. Consider the Hamiltonian for a general K-state system with d nuclear degrees of freedom in the diabatic representation:

$$\hat{H} = \sum_{j=1}^{d} \frac{\hat{P}_j^2}{2M_j} + \sum_{n,m=1}^{K} |n\rangle V_{nm}(\hat{\mathbf{R}})\langle m|. \tag{3.1}$$

In Eq. (3.1), $\hat{\mathbf{R}}$ and $\hat{\mathbf{P}}$ represent nuclear position and momentum operators, respectively, M is nuclear mass, $\{|n\rangle\}$ are diabatic electronic states, and $\{V_{nm}(\mathbf{R})\}$ are diabatic potential energy matrix elements. PI discretization of the corre-

sponding partition function involves inserting copies of the identity operator represented in the product space of diabatic electronic states and nuclear positions, $\hat{\mathbb{1}} = \int d\mathbf{R} \sum_n |\mathbf{R}, n\rangle\langle\mathbf{R}, n|$, such that

$$Z = \mathrm{Tr}\left[e^{-\beta\hat{H}}\right] = \lim_{N\to\infty} \int \{d\mathbf{R}_\alpha\} \sum_{\{n_\alpha\}=1}^{K} \prod_{\alpha=1}^{N} \langle \mathbf{R}_\alpha, n_\alpha | e^{-\frac{\beta}{N}\hat{\mathbf{V}}} e^{-\frac{\beta}{N}\hat{K}} | \mathbf{R}_{\alpha+1}, n_{\alpha+1}\rangle. \tag{3.2}$$

Above, $\hat{\mathbf{V}}$ represents the diabatic potential energy operator, $(\mathbf{R}_\alpha, n_\alpha)$ refers to the nuclear position and electronic state of the α^{th} bead, $(\mathbf{R}_{N+1}, n_{N+1}) = (\mathbf{R}_1, n_1)$, and we use the notations $\int \{d\mathbf{R}_\alpha\} = \int d\mathbf{R}_1 \int d\mathbf{R}_2 \ldots \int d\mathbf{R}_N$ and $\sum_{\{n_\alpha\}=1}^{K} = \sum_{n_1=1}^{K} \sum_{n_2=1}^{K} \cdots \sum_{n_N=1}^{K}$.

Further inserting copies of identity in momentum space allows us to evaluate kinetic energy operators. We can also generate simple expressions for the potential energy matrix elements by expanding the off-diagonal exponential terms to second order in β/N such that

$$\langle n_\alpha | e^{-\frac{\beta}{N}\hat{\mathbf{V}}(\mathbf{R}_\alpha)} | n_{\alpha+1}\rangle \approx [\mathbf{M}(\mathbf{R}_\alpha)]_{n_\alpha n_{\alpha+1}}, \tag{3.3}$$

where the $K \times K$-dimensional nuclear-electronic interaction matrix $\mathbf{M}$ has elements [62]

$$[\mathbf{M}(\mathbf{R}_\alpha)]_{n_\alpha n_{\alpha+1}} = \begin{cases} e^{-\frac{\beta}{N} V_{n_\alpha n_\alpha}(\mathbf{R}_\alpha)} & n_\alpha = n_{\alpha+1} \\ -\frac{\beta}{N} V_{n_\alpha n_{\alpha+1}}(\mathbf{R}_\alpha)\, e^{-\frac{\beta}{N} V_{n_\alpha n_\alpha}(\mathbf{R}_\alpha)} & n_\alpha \neq n_{\alpha+1}. \end{cases} \tag{3.4}$$

Once again multiplying by normalized Gaussian momentum integrals for the nuclear degrees of freedom, we arrive at an expression for the partition function in the state space PI framework [4]:

$$Z = \lim_{N\to\infty} \left(\frac{1}{2\pi\hbar}\right)^{dN} \int \{d\mathbf{R}_\alpha\} \int \{d\mathbf{P}_\alpha\}\, e^{-\frac{\beta}{N} H_{MF}(\{\mathbf{R}_\alpha, \mathbf{P}_\alpha\})}, \tag{3.5}$$

where

$$H_{MF} = \sum_{j=1}^{d} \sum_{\alpha=1}^{N} \left[\frac{P_{j,\alpha}^2}{2M_j} + \frac{M_j N^2}{2\beta^2\hbar^2}(R_{j,\alpha} - R_{j,\alpha+1})^2\right] - \frac{N}{\beta}\ln\left(\mathrm{Tr}\left[\Gamma\right]\right) \tag{3.6}$$

and Γ represents a product of the interaction matrices for all beads,

$$\Gamma = \prod_{\alpha=1}^{N} \mathbf{M}(\mathbf{R}_\alpha). \tag{3.7}$$

Note that the trace of Γ is positive for all K-level systems when the off-diagonal diabatic coupling matrix elements are positive (as in all cases considered here). Finally, the canonical ensemble average of an observable in the state space PI framework is written in a similar fashion,

$$\left\langle \hat{A} \right\rangle = \frac{1}{Z}\mathrm{Tr}[e^{-\beta\hat{H}}A(\hat{\mathbf{R}})] = \lim_{N\to\infty} \frac{\int \{d\mathbf{R}_\alpha\} \int \{d\mathbf{P}_\alpha\}\, e^{-\frac{\beta}{N}H_{MF}(\{\mathbf{R}_\alpha,\mathbf{P}_\alpha\})} A_N(\{\mathbf{R}_\alpha\})}{\int \{d\mathbf{R}_\alpha\} \int \{d\mathbf{P}_\alpha\}\, e^{-\frac{\beta}{N}H_{MF}(\{\mathbf{R}_\alpha,\mathbf{P}_\alpha\})}}, \tag{3.8}$$

and can be evaluated exactly using standard PIMC or PIMD techniques.

3.2 Mean Field Ring Polymer Molecular Dynamics

Although electronic variables appear implicitly in the elements of the nuclear-electronic interaction matrix, Eq. (3.4), the Hamiltonian in Eq. (3.6) describes nuclear dynamics on a mean potential energy surface. The RPMD extension of Eq. (3.8) is therefore called mean field RPMD, and correlation functions are expressed as

$$\widetilde{C}_{AB}^{MF}(t) \approx \lim_{N\to\infty} \frac{1}{Z}\left(\frac{1}{2\pi\hbar}\right)^{dN} \int \{d\mathbf{R}_\alpha\} \int \{d\mathbf{P}_\alpha\}\, e^{-\frac{\beta}{N}H_{MF}} A_N(0) B_N(t). \tag{3.9}$$

Mean field dynamics are exact for equilibrium expectation values and allow us to, for example, calculate the average equilibrium population of electronic state n exactly from the expression

$$\left\langle \hat{\mathbb{P}}_n \right\rangle = \frac{1}{Z}\mathrm{Tr}[e^{-\beta\hat{H}}\hat{\mathbb{P}}_n] = \lim_{N\to\infty} \frac{\int \{d\mathbf{R}_\alpha\} \int \{d\mathbf{P}_\alpha\}\, e^{-\frac{\beta}{N}H_{MF}(\{\mathbf{R}_\alpha,\mathbf{P}_\alpha\})} \frac{\mathrm{Tr}[\Gamma\mathbb{P}_n]}{\mathrm{Tr}[\Gamma]}}{\int \{d\mathbf{R}_\alpha\} \int \{d\mathbf{P}_\alpha\}\, e^{-\frac{\beta}{N}H_{MF}(\{\mathbf{R}_\alpha,\mathbf{P}_\alpha\})}}, \tag{3.10}$$

where $\hat{\mathbb{P}}_n = |n\rangle\langle n|$ represents the projection operator onto state 1. However, mean field RPMD cannot describe dynamical transitions between electronic states—dynamics on a single mean potential energy surface cannot resolve individual states—and fails to capture accurate nuclear dynamics in certain regimes of electronic coupling.

More specifically, MF-RPMD has been shown to work well for systems involving strongly-coupled electronic states (the adiabatic regime), but it breaks down for weakly-coupled states (the nonadiabatic regime) due to the neglect of fluctuations in electronic state variables [6, 27]. As a result, MF-RPMD has been largely overlooked as a viable method for the simulation of nonadiabatic charge and energy transfer reactions in the condensed phase. However, in the remainder of this chapter, we show that properly exploiting the implicit state information in MF-RPMD allows us to obtain surprisingly accurate results for reaction rates in the strong *and* weak coupling regimes.

3.3 Re-weighting the Solvent Reaction Coordinate

Consider again the Bennett-Chandler rate constant,

$$k = \frac{\left\langle \dot{\xi}_0 \, h\left(\dot{\xi}_0\right)\right\rangle_c \left\langle \delta\left(\xi_0 - \xi^\ddagger\right)\right\rangle}{\left\langle h\left(\xi^\ddagger - \xi_0\right)\right\rangle} \times \lim_{t\to\infty} \frac{\left\langle \dot{\xi}_0 \, h\left(\xi_t - \xi^\ddagger\right)\right\rangle_c}{\left\langle \dot{\xi}_0 \, h\left(\dot{\xi}_0\right)\right\rangle_c \left\langle \delta\left(\xi_0 - \xi^\ddagger\right)\right\rangle}, \tag{3.11}$$

which describes the rate of a reaction in terms of a one-dimensional reaction coordinate ξ. For clarity, we will discuss ξ in the context of standard system-bath models for electron transfer (ET), where a two-state system is coupled to a dissipative bath via a single collective solvent coordinate (Fig. 3.1), but the ideas presented here are easily generalized. The traditional mean field RPMD approach

defines ξ purely as a function of the nuclear (i.e. solvent) ring polymer center of mass (COM), $\xi \equiv \overline{\mathbf{R}} = \sum_{\alpha=1}^{N} \mathbf{R}_\alpha / N$, such that the transition state, reactant basin, and product basin correspond to $\overline{\mathbf{R}} = \mathbf{R}^\ddagger$, $\overline{\mathbf{R}} \leq \mathbf{R}^\ddagger$, and $\overline{\mathbf{R}} > \mathbf{R}^\ddagger$, respectively, with $\mathbf{R}^\ddagger$ indicating the point of degeneracy between the two diabatic potential energy curves. As expected, rate constants calculated using this coordinate are accurate in the adiabatic limit but severely overestimate rates in the nonadiabatic limit because they neglect the probability of forming *electronic* transition states, the magnitude of which is proportional to the electronic coupling squared [1]. Use of this coordinate is of course also limited to the "normal" regime of ET where the minima of the reactant and product diabats lie on opposite sides of $\mathbf{R}^\ddagger$.

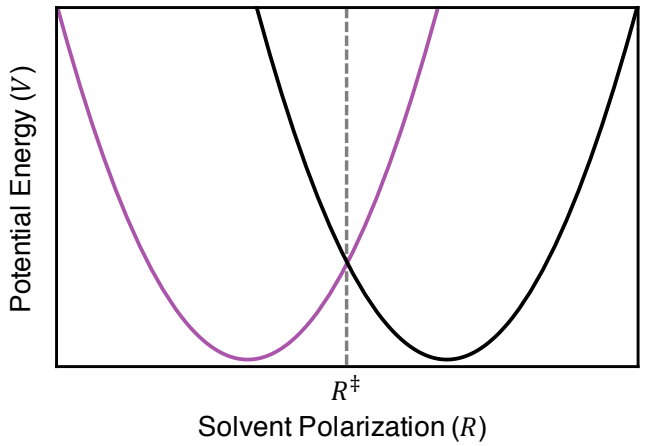

Figure 3.1: An illustration of a two-state electron transfer system in the diabatic representation (bath not shown). The purple (left) and black (right) curves represent the reactant and product states, respectively, as a function of the collective solvent polarization coordinate. The point $R^\ddagger$ (gray dotted line) corresponds to the solvent position at which the diabats intersect and represents the transition state along this coordinate.

The lack of explicit electronic variables in the mean surface dynamics makes the solvent coordinate seem like the best, if not the only, choice for describing reaction progress. However, MF-RPMD is only used to calculate the dynamic recrossing factor, $\kappa(t)$, which for a properly chosen transition state should

contribute minimally to the magnitude of the total rate constant. In contrast, k_{TST} represents a purely statistical term that can be solved with either PIMC or PIMD and does not suffer from the same limitations as the MF-RPMD simulation. With this in mind, in a preliminary attempt to improve MF-RPMD rates in the nonadiabatic limit, we keep the solvent coordinate as our primary reaction coordinate but correct the k_{TST} term to account for the additional probability of forming electronic transition states, $n^{\ddagger}$. Our new definition of k_{TST} becomes

$$k_{\mathrm{TST}} = \left\langle \dot{\overline{\mathbf{R}}}_0 \, h\left(\dot{\overline{\mathbf{R}}}_0\right) \right\rangle_c \times \mathrm{P}\left(\mathbf{R}^{\ddagger}, n^{\ddagger}\right), \tag{3.12}$$

which represents the product of the average forward velocity and the TS probability, where the TS used here involves a simultaneous restraint on nuclear and electronic configurations. As such, $\langle \cdots \rangle_c$ now indicates an ensemble average with the system constrained to the total nuclear-electronic TS, and the probability of reaching this TS from reactant configurations is

$$\mathrm{P}\left(\mathbf{R}^{\ddagger}, n^{\ddagger}\right) = \frac{\int \{d\mathbf{R}_\alpha\} \, e^{-\frac{\beta}{N} H'_{MF}(\{\mathbf{R}_\alpha\})} \mathrm{Tr}\left[\Gamma_{\mathrm{kinks}}\right] \delta\left(\overline{\mathbf{R}} - \mathbf{R}^{\ddagger}\right)}{\int_{-\infty}^{\mathbf{R}^{\ddagger}} d\mathbf{R}' \int \{d\mathbf{R}_\alpha\} \, e^{-\frac{\beta}{N} H'_{MF}(\{\mathbf{R}_\alpha\})} \mathrm{Tr}\left[\Gamma \mathbb{P}_1\right] \delta\left(\overline{\mathbf{R}} - \mathbf{R}'\right)}, \tag{3.13}$$

where

$$H'_{MF} = \sum_{j=1}^{d} \sum_{\alpha=1}^{N} \left[\frac{M_j N^2}{2\beta^2 \hbar^2} (R_{j,\alpha} - R_{j,\alpha+1})^2 \right]. \tag{3.14}$$

In Eq. (3.13), Γ refers to the nuclear-electronic state interaction term previously defined in Eq. (3.7) that accounts for all possible electronic state configurations. Γ_{kinks} represents a subset of Γ that includes only "kinked" ring polymer configurations where at least one bead is in a different electronic state than the others. As illustrated in Fig. 3.2, the cyclicity of a ring polymer ensures that kinks appear in pairs, so the phrase "kink-pairs" is often used when describing these types of configurations. Physically, kink-pair configurations represent electronic transition or tunneling states in the state space ring polymer picture,

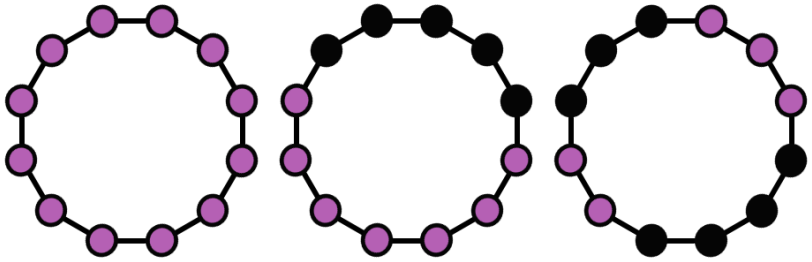

Figure 3.2: An illustration of ring polymer configurations with zero (left), one (center), and two (right) kink-pairs in a two-state system. The colors purple and black represent the two states of the system.

and by combining them with a restraint on the solvent COM to $\mathbf{R}^{\ddagger}$, the numerator in Eq. (3.13) describes an average over full nuclear-electronic TS configurations. Further, the projection matrix $\mathbb{P}_1$ in Eq. (3.13) projects the N^{th} electronic ring polymer bead onto state 1 so that $\Gamma\mathbb{P}_1$ accounts for ring polymer configurations where all beads are in the reactant electronic state as well as kinked configurations. The denominator thus represents an average over reactant state configurations.

Finally, for consistency we reformulate $\kappa(t)$ to involve an initial constraint to the TS described above, denoted by $\langle\cdots\rangle_c$, but otherwise calculate recrossing exclusively as a function of the solvent degree of freedom:

$$\kappa_{\text{MF-RPMD}}(t) = \lim_{t\to\infty} \frac{\left\langle \dot{\overline{\mathbf{R}}}_0 \, h\left(\overline{\mathbf{R}}_t - \mathbf{R}^{\ddagger}\right)\right\rangle_c}{\left\langle \dot{\overline{\mathbf{R}}}_0 \, h\left(\dot{\overline{\mathbf{R}}}_0\right)\right\rangle_c}. \tag{3.15}$$

The specifics of calculating k_{TST} and $\kappa_{\text{MF-RPMD}}(t)$ are described in the next section.

3.3.1 Implementation Details

In practice, it is easiest to evaluate the probability of forming TS configurations by splitting Eq. (3.13) into two terms:

$$\mathrm{P}\left(\mathbf{R}^{\ddagger}, n^{\ddagger}\right) = \mathrm{P}\left(\mathbf{R}^{\ddagger}\right) \times \mathrm{P}\left(n^{\ddagger}|\mathbf{R}^{\ddagger}\right), \tag{3.16}$$

where

$$\mathrm{P}\left(\mathbf{R}^{\ddagger}\right) = \frac{\int \{d\mathbf{R}_{\alpha}\}\, e^{-\frac{\beta}{N} H'_{MF}(\{\mathbf{R}_{\alpha}\})} \mathrm{Tr}\left[\Gamma \mathbb{P}_1\right] \delta\left(\overline{\mathbf{R}} - \mathbf{R}^{\ddagger}\right)}{\int_{-\infty}^{\mathbf{R}^{\ddagger}} d\mathbf{R}' \int \{d\mathbf{R}_{\alpha}\}\, e^{-\frac{\beta}{N} H'_{MF}(\{\mathbf{R}_{\alpha}\})} \mathrm{Tr}\left[\Gamma \mathbb{P}_1\right] \delta\left(\overline{\mathbf{R}} - \mathbf{R}'\right)} \tag{3.17}$$

represents the probability of the system reaching the nuclear TS, $\overline{\mathbf{R}} = \mathbf{R}^{\ddagger}$, from the reactant state, and

$$\mathrm{P}\left(n^{\ddagger}|\mathbf{R}^{\ddagger}\right) = \frac{\int \{d\mathbf{R}_{\alpha}\}\, e^{-\frac{\beta}{N} H'_{MF}(\{\mathbf{R}_{\alpha}\})} \mathrm{Tr}\left[\Gamma_{\mathrm{kinks}}\right] \delta\left(\overline{\mathbf{R}} - \mathbf{R}^{\ddagger}\right)}{\int \{d\mathbf{R}_{\alpha}\}\, e^{-\frac{\beta}{N} H'_{MF}(\{\mathbf{R}_{\alpha}\})} \mathrm{Tr}\left[\Gamma \mathbb{P}_1\right] \delta\left(\overline{\mathbf{R}} - \mathbf{R}^{\ddagger}\right)} \tag{3.18}$$

represents the conditional probability of the system forming the electronic TS (kink-pair configurations) given that the solvent COM is positioned at $\mathbf{R}^{\ddagger}$. We evaluate Eq. (3.17) by generating a free energy profile along $\overline{\mathbf{R}}$ using umbrella sampling [64] and the weighted histogram analysis method [65], where a harmonic restraint on $\overline{\mathbf{R}}$ is used to center simulation windows at different values $\mathbf{R}_i$ throughout the reactant and TS regions. In each window, nuclear configurations are generated by Monte Carlo (MC) importance sampling using the weighting function

$$W_1 = e^{-\frac{\beta}{N} H'_{MF} - \frac{1}{2} k_c \left(\overline{\mathbf{R}} - \mathbf{R}_i\right)^2} \mathrm{Tr}\left[\Gamma \mathbb{P}_1\right]. \tag{3.19}$$

In a separate simulation, we evaluate Eq. (3.18) via importance sampling using the weighting function

$$W_2 = e^{-\frac{\beta}{N} H'_{MF}}, \tag{3.20}$$

and the delta function $\delta\left(\overline{\mathbf{R}} - \mathbf{R}^{\ddagger}\right)$ is enforced by shifting the nuclear ring polymer COM to $\mathbf{R}^{\ddagger}$ before calculating the potential at each MC step. The terms $\mathrm{Tr}\left[\Gamma_{\mathrm{kinks}}\right]$

and $\mathrm{Tr}\left[\Gamma\mathbb{P}_1\right]$ are evaluated for each accepted configuration, and the ratio of their final averages yields $\mathrm{P}\left(n^{\ddagger}|\mathbf{R}^{\ddagger}\right)$.

Calculating $\mathrm{Tr}\left[\Gamma_{\mathrm{kinks}}\right]$ and $\mathrm{Tr}\left[\Gamma\mathbb{P}_1\right]$ involves generating subsets of Γ, which we accomplish by inserting appropriate projection matrices between the $\mathbf{M}$ matrices in Eq. (3.7). For instance, $\Gamma\mathbb{P}_1$ is calculated from

$$\Gamma\mathbb{P}_1 = \left(\prod_{\alpha=1}^{N}\mathbf{M}(\mathbf{R}_\alpha)\right)\mathbb{P}_1 \tag{3.21}$$

with

$$\mathbb{P}_1 = \begin{bmatrix} 1 & 0 \\ 0 & 0 \end{bmatrix}. \tag{3.22}$$

Similarly, Γ_{kinks} is most easily calculated by subtracting from Γ configurations where all beads are in the same state. Considering a two-state system for simplicity,

$$\Gamma_{\mathrm{kinks}} = \Gamma - \prod_{\alpha=1}^{N}\left(\mathbf{M}(\mathbf{R}_\alpha)\mathbb{P}_1\right) - \prod_{\alpha=1}^{N}\left(\mathbf{M}(\mathbf{R}_\alpha)\mathbb{P}_2\right), \tag{3.23}$$

where

$$\mathbb{P}_2 = \begin{bmatrix} 0 & 0 \\ 0 & 1 \end{bmatrix}. \tag{3.24}$$

The average forward velocity term that appears in the numerator of the TST estimate and the denominator of the dynamic recrossing factor can be analytically obtained by evaluating a Gaussian integral in the solvent momentum,

$$\left\langle \dot{\bar{\mathbf{R}}}_0\, h\left(\dot{\bar{\mathbf{R}}}_0\right)\right\rangle_c = \left(\frac{1}{2\pi\beta M}\right)^{d/2}. \tag{3.25}$$

Initial configurations for MF-RPMD trajectories are generated by importance sampling using the weighting function

$$W_3 = e^{-\frac{\beta}{N}H'_{MF}}\mathrm{Tr}\left[\Gamma_{\mathrm{kinks}}\right], \tag{3.26}$$

and the delta function $\delta\left(\overline{\mathbf{R}} - \mathbf{R}^{\ddagger}\right)$ is, as before, enforced by shifting the nuclear COM to $\mathbf{R}^{\ddagger}$ after each MC step. MF-RPMD trajectories are then evolved in time using the classical ring polymer Hamiltonian in Eq. (3.6); averaging the expression $\left(\dot{\overline{\mathbf{R}}}_0\, h\left(\overline{\mathbf{R}}_t - \mathbf{R}^{\ddagger}\right)\right)$ over all trajectories and dividing by Eq. (3.25) gives us a value for $\kappa_{\text{MF-RPMD}}$.

3.3.2 Model Systems

In the following sections, we benchmark the approach outlined above using condensed-phase single electron transfer systems with potential energy functions of the form [27, 66]

$$V\left(\hat{\mathbf{R}}\right) = V_S\left(\hat{\mathbf{R}}\right) + \hat{\mathbb{1}} V_B\left(\hat{\mathbf{R}}\right), \tag{3.27}$$

where $\hat{\mathbb{1}}$ is the identity matrix and $\mathbf{R} = \{s, \mathbf{Q}\}$ represents the full set of nuclear coordinates, including both a solvent polarization coordinate, s, and bath coordinates, $\mathbf{Q}$. The diabatic potential energy matrix for each system, constructed along the solvent coordinate, has the form

$$V_S\left(\hat{\mathbf{R}}\right) = \begin{bmatrix} A\hat{s}^2 + B\hat{s} + \epsilon & \Delta \\ \Delta & A\hat{s}^2 - B\hat{s} \end{bmatrix}, \tag{3.28}$$

and the solvent coordinate, with associated mass M_S, is linearly coupled to a bath of f harmonic oscillators, each with mass M_B, through the potential

$$V_B\left(\hat{\mathbf{R}}\right) = \sum_{j=1}^{f} \left[\frac{1}{2} M_B \omega_j^2 \left(\hat{Q}_j - \frac{c_j \hat{s}}{M_B \omega_j^2} \right)^2 \right]. \tag{3.29}$$

The spectral density of the bath is Ohmic,

$$J(\omega) = \eta \omega e^{-\omega/\omega_c}, \tag{3.30}$$

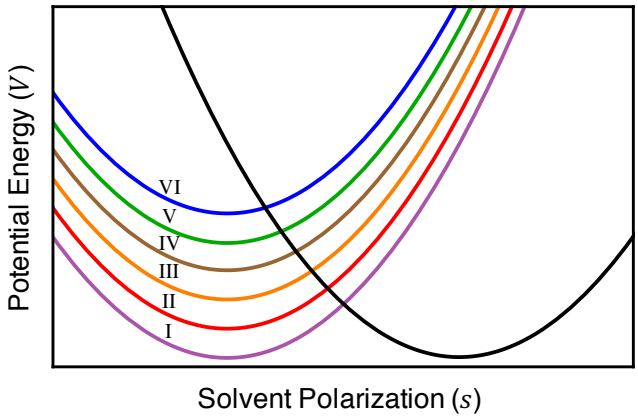

Figure 3.3: Electron transfer model systems with varying driving force. Models I - VI correspond to the purple, red, orange, brown, green, and blue diabats, respectively. In each case, the left curve represents the reactant state, and the right (black) curve represents the product state. Note that each model is in the Marcus normal regime of ET, where the diabatic states intersect at a point that lies between the minima of the two states.

with cutoff frequency ω_c and dimensionless parameter η that determines the friction strength of the bath. Following the scheme developed in Ref. 34, we discretize this spectral density into f oscillators with frequencies

$$\omega_j = -\omega_c \ln\left(\frac{j - 1/2}{f}\right) \tag{3.31}$$

and coupling strengths

$$c_j = \omega_j \left(\frac{2\eta M_B \omega_c}{f\pi}\right)^{1/2}, \tag{3.32}$$

where $j = 1...f$. Within these systems, we test a range of driving force values, ϵ, as well as a range of electronic coupling strengths, Δ, from the nonadiabatic to the adiabatic limit. Parameters for these models are reported in Tables 3.1 and 3.2, and the diabatic state potential energy curves are plotted in Fig. 3.3.

Table 3.1: Parameters for the system-bath ET models. Unless otherwise specified, values are reported in atomic units.

Parameter	Value
A	4.772×10^{-3}
B	2.288×10^{-2}
M_S	1836.0
M_B	1836.0
f	12
ω_c	2.28×10^{-3}
$\eta/M_B\omega_c$	1.0
T	300 K

Table 3.2: Driving force and coupling parameters for the ET model systems. All values are reported in atomic units.

Model	ϵ	Δ
I	0.0000	6.69×10^{-7} - 1.20×10^{-2}
II	0.0146	6.69×10^{-7}
III	0.0296	6.69×10^{-7}
IV	0.0446	6.69×10^{-7}
V	0.0586	6.69×10^{-7}
VI	0.0738	6.69×10^{-7}

3.3.3 Alternative Rate Theories

For these simple model systems, we compare our MF-RPMD rates to the relevant rate theories described below in order to gauge our accuracy in the various parameter regimes. The nonadiabatic (i.e. weak coupling) ET rate for a quantized solvent can be calculated using Fermi's golden rule (FGR) [67]. For systems like those described in Section 3.3.2 where the reactant and product diabatic potential energy surfaces are displaced harmonic oscillators with frequency ω_s, FGR rates take the simple analytical form [68, 69]

$$k_{\mathrm{FGR}} = \frac{2\pi}{\hbar\omega_s}|\Delta|^2 e^{v z - S\ \coth(z)} I_v\left(S\ \operatorname{csch}(z)\right), \tag{3.33}$$

where $z = \beta\omega_s/2$, $v = \epsilon/\omega_s$, $S = M_s\omega_s V_d^2/2\hbar$, M_S is the solvent mass, I_v is a modified Bessel function of the first kind, and V_d is the horizontal displacement

of the diabatic potential energy functions. Reaction rates for ET in the adiabatic (i.e. strong coupling) limit with a quantum solvent can be estimated using Kramers theory (KT) [70],

$$k_{\mathrm{KT}} = \left(\sqrt{1 + \left(\frac{\gamma}{2\omega_b} \right)^2} - \frac{\gamma}{2\omega_b} \right) \frac{\omega_s}{2\pi} e^{-\beta G^{\ddagger}_{\mathrm{cl}}}, \tag{3.34}$$

where ω_b is the frequency at the barrier top, $G^{\ddagger}_{\mathrm{cl}}$ is the solvent FE barrier when the solvent is treated classically, $\gamma = \eta/M_S$ [71], and η is the strength of coupling to a dissipative bath.

3.3.4 Results

For the model systems described in Section 3.3.2, we now compare reaction rate constants calculated using our modified MF-RPMD rate theory to those predicted by FGR and Kramers theory. In each case considered, all degrees of freedom in the PI simulations are quantized with $N = 32$ ring polymer beads. For the k_{TST} calculation, we umbrella sample using 60 windows spaced evenly in the range $-6 < s < 0.5$ and constrained with a force constant $k_c = 200$ a.u. $\kappa_{\text{MF-RPMD}}(t)$ results are obtained by averaging over $24,000$ trajectories evolved using a fourth-order Adams-Bashforth-Moulton predictor-corrector integrator and a time step $dt = 0.1$ a.u.

We first consider the symmetric ET system, Model I ($\epsilon = 0$), and a range of coupling strengths between the electronic states. Fig. 3.4 shows MF-RPMD results plotted against Kramers theory rates for adiabatic ET and FGR rates for nonadiabatic transfer. As hoped, MF-RPMD rates exhibit quantitative agreement with FGR rates in the weak coupling regime and transition to following the Kramers theory curve as the coupling increases. Numerical values for these

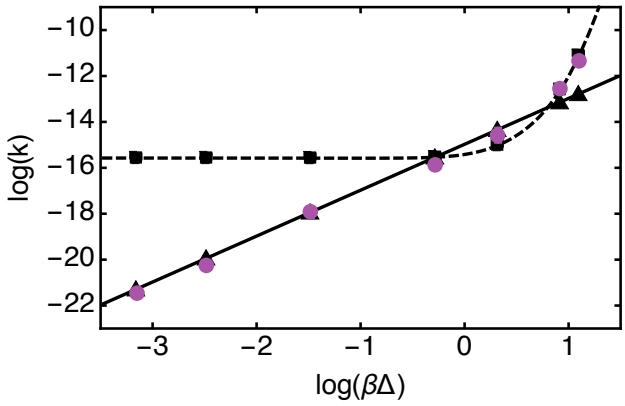

Figure 3.4: Electron transfer rate constants for a range of electronic coupling constants, Δ, in the symmetric model ($\epsilon = 0$). MF-RPMD values are shown in purple dots, FGR rate constants are shown in black triangles and a solid black line, and Kramers theory rate constants are shown in black squares and a black dashed line. Both axes are reported in atomic units.

rate constants are also reported in Table 3.3, along with the isolated TST rates—we see that, despite the limitations of MF-RPMD, the accuracy of the TST rates in this regime is sufficient for good numerical agreement.

Table 3.3: Electron transfer rate constants for a range of electronic coupling strengths, Δ, in the symmetric model ($\epsilon = 0$). From left to right, the four rightmost columns report the TST estimate to the rate constant, the full MF-RPMD rate constant, Fermi's golden rule values, and Kramers theory rate constants, respectively. The numbers in parentheses represent the statistical uncertainty in the last digit shown, and all values are reported in atomic units.

Δ	$\log(k_{\text{TST}})$	$\log(k_{\text{MF-RPMD}})$	$\log(k_{\text{FGR}})$	$\log(k_{\text{KT}})$
6.69×10^{-7}	-21.47	-21.47(8)	-21.28	-15.57
3.16×10^{-6}	-20.22	-20.2(2)	-19.93	-15.58
3.16×10^{-5}	-17.95	-17.9(2)	-17.93	-15.58
5.01×10^{-4}	-15.84	-15.8(1)	-15.53	-15.54
2.00×10^{-3}	-14.55	-14.6(3)	-14.33	-15.02
7.94×10^{-3}	-12.51	-12.55(4)	-13.13	-12.60
1.20×10^{-2}	-11.30	-11.3(2)	-12.77	-11.11

We next fix the electronic coupling to the lowest value considered above (traditionally the most troublesome regime for MF-RPMD) and explore a range of driving forces (Models I-VI). Fig. 3.5 compares our MF-RPMD rates to FGR

rates, and the numerical values of these rate constants are reported in Table 3.4, along with the isolated TST estimates. The dynamic recrossing factor as a function of time is also plotted in Fig. 3.6. Again we find that our MF-RPMD imple-

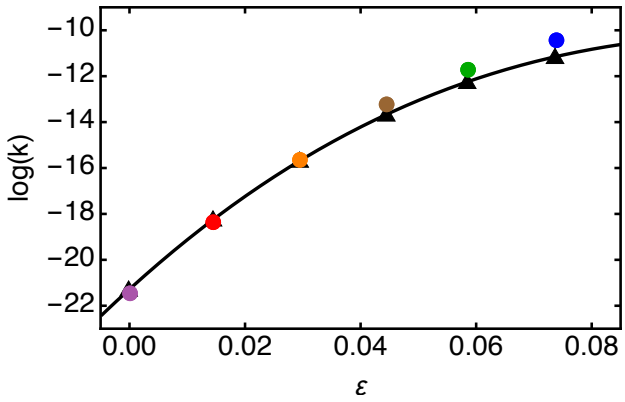

Figure 3.5: Electron transfer rate constants computed for a range of driving force values, ϵ, with constant coupling $\Delta = 6.69 \times 10^{-7}$ a.u. Colored dots correspond to MF-RPMD results, and the black triangles as well as the solid black line correspond to FGR rate constants. Both axes are reported in atomic units.

mentation proves quantitatively accurate for ET in the normal regime. The high values of $\kappa_{\text{MF-RPMD}}(t)$, particularly for the symmetric and near-symmetric models of ET, demonstrate the accuracy of our TST rates for these systems. As the models become more asymmetric, $\kappa_{\text{MF-RPMD}}$ decreases, and eventually, as seen in Model VI (blue curve), we no longer observe plateau behavior at longer times (we use the value of $\kappa_{\text{MF-RPMD}}$ at $t = 8000$ a.u. to obtain the reported rate constant for this model). Beyond Model VI, the solvent coordinate becomes invalid since it fails to distinguish between reactant and product states.

3.4 Introducing the Population Reaction Coordinate

In the previous section, we showed that incorporating the additional probability of forming electronic transition states into the MF-RPMD rate equation allows

Table 3.4: Electron transfer rate constants computed for a range of driving forces, ϵ, with constant coupling $\Delta = 6.69 \times 10^{-7}$ a.u. From left to right, the three rightmost columns report the TST estimate to the rate constant, the full MF-RPMD rate constant, and the Fermi's golden rule values, respectively. The numbers in parentheses represent the statistical uncertainty in the last digit shown, and all values are reported in atomic units.

Model	ϵ	$\log(k_{\text{TST}})$	$\log(k_{\text{MF-RPMD}})$	$\log(k_{\text{FGR}})$
I	0.0000	-21.47	-21.47(8)	-21.28
II	0.0146	-18.35	-18.349(6)	-18.23
III	0.0296	-15.65	-15.670(5)	-15.66
IV	0.0446	-13.18	-13.22(1)	-13.65
V	0.0586	-11.60	-11.69(1)	-12.23
VI	0.0738	-10.18	-10.47(8)	-11.15

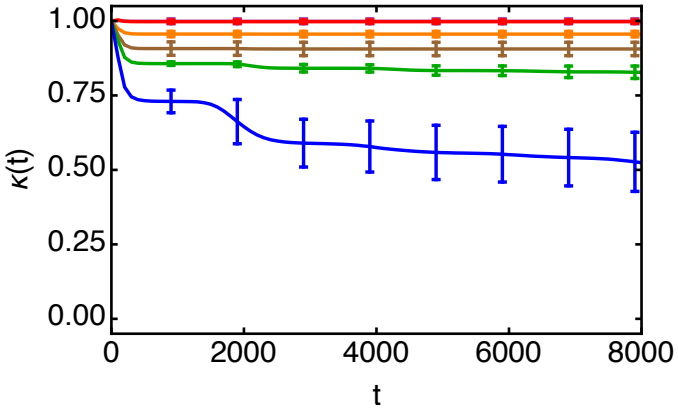

Figure 3.6: Plots of the dynamical recrossing term, $\kappa_{\text{MF-RPMD}}(t)$, computed using the solvent reaction coordinate as a function of time for Models I-VI (purple, red, orange, brown, green, and blue, respectively). All values are reported in atomic units.

us to predict accurate rate constants in the weak coupling regime of electron transfer. However, the approach we described is not ideal because it involves an inconsistent definition of the transition state and flux-side coordinate, with the former being two-dimensional and the latter one-dimensional. Moreover, employing the solvent coordinate as the primary reaction coordinate limits the method's applicability to the normal regime of ET. Here we address both of these problems by introducing a new reaction coordinate, $\xi \equiv \Delta\mathbb{P}$, that describes reaction progress as a function of the difference between the bead populations

of the two electronic states. This coordinate naturally distinguishes between reactant, TS, and product configurations in all regimes of ET, including the "inverted" regime, where the minima of both electronic states lie on the same side of $\mathbf{R}^\ddagger$:

$$\Delta\mathbb{P} = \begin{cases} -1 & \text{reactant minimum} \\ 0 & \text{transition state} \\ 1 & \text{product minimum.} \end{cases} \tag{3.35}$$

The transition state along this "population coordinate" corresponds to configurations that have an equal number of beads in the reactant and product states, and we express the probability of reaching such a transition state from the reactant state as

$$\mathrm{P}\left(\mathbf{R}^\ddagger, n^\ddagger\right) = \frac{\int \{d\mathbf{R}_\alpha\}\, e^{-\frac{\beta}{N} H'_{MF}(\{\mathbf{R}_\alpha\})} \mathrm{Tr}\left[\Gamma_{\Delta\mathbb{P}=0}\right] \delta\left(\overline{\mathbf{R}} - \mathbf{R}^\ddagger\right)}{\int \{d\mathbf{R}_\alpha\}\, e^{-\frac{\beta}{N} H'_{MF}(\{\mathbf{R}_\alpha\})} \mathrm{Tr}\left[\Gamma_{\Delta\mathbb{P}=-1}\right]}, \tag{3.36}$$

where $\Gamma_{\Delta\mathbb{P}=0}$ includes only kinked configurations with an equal number of ring polymer beads in either state and $\Gamma_{\Delta\mathbb{P}=-1}$ includes only configurations where all ring polymer beads are in the reactant state. Note that in the numerator of Eq. (3.36), we have restricted the solvent COM to $\mathbf{R}^\ddagger$ so that kinks can only form at the diabatic crossing point—this approximation allows us to overcome a known failure of the RPMD method, where transitions between potential wells in the inverted regime appear with unphysically large probabilities [42]. (To see this, consider that $\mathrm{Tr}\left[\Gamma_{\Delta\mathbb{P}=-1}\right]$ contains only terms involving the higher-energy state, $e^{-\frac{\beta}{N} V_{11}(\mathbf{R}_\alpha)}$, whereas $\mathrm{Tr}\left[\Gamma_{\Delta\mathbb{P}=0}\right]$ contains some terms involving the lower-energy state, $e^{-\frac{\beta}{N} V_{22}(\mathbf{R}_\alpha)}$. As a result, $\mathrm{Tr}\left[\Gamma_{\Delta\mathbb{P}=0}\right] > \mathrm{Tr}\left[\Gamma_{\Delta\mathbb{P}=-1}\right]$ for $\overline{\mathbf{R}} > \mathbf{R}^\ddagger$ in the inverted regime, making kinked configurations unphysically more favorable than the reactant state unless a constraint on kink formation is introduced.) Menzeleev et al. employ a more rigorous version of this constraint in their kinetically constrained (KC)-RPMD method [42], but for our first pass with the population

estimator we wish to minimize the computational complexity.

We write the full k_{TST} term as

$$k_{\mathrm{TST}} = \left\langle \Delta\dot{\mathbb{P}}_0 \; h\left(\Delta\dot{\mathbb{P}}_0\right)\right\rangle_c \times \mathrm{P}\left(\mathbf{R}^{\ddagger}, n^{\ddagger}\right), \tag{3.37}$$

where $\mathrm{P}\left(\mathbf{R}^{\ddagger}, n^{\ddagger}\right)$ is defined in Eq. (3.36) and $\langle \cdots \rangle_c$ represents an initial constraint to configurations with half of the beads in one state and half in the other and where the solvent COM is positioned at the diabatic crossing point. The recrossing factor is likewise expressed as a function of this new population coordinate:

$$\kappa_{\text{MF-RPMD}}\left(t\right) = \lim_{t\to\infty} \frac{\left\langle \Delta\dot{\mathbb{P}}_0 \; h\left(\Delta\mathbb{P}_t\right)\right\rangle_c}{\left\langle \Delta\dot{\mathbb{P}}_0 \; h\left(\Delta\dot{\mathbb{P}}_0\right)\right\rangle_c}. \tag{3.38}$$

Because the mean field dynamics do not provide a way to explicitly track electronic state population dynamics, in Eqs. (3.37) and (3.38) we use an approximate definition of $\Delta\mathbb{P}$ based on the normalized difference between the equilibrium population estimators of the two states (see Eq. (3.10)):

$$\Delta\mathbb{P} = \frac{\mathrm{Tr}[\Gamma\mathbb{P}_2] - \mathrm{Tr}[\Gamma\mathbb{P}_1]}{\mathrm{Tr}[\Gamma\mathbb{P}_2] + \mathrm{Tr}[\Gamma\mathbb{P}_1]}. \tag{3.39}$$

3.4.1 Implementation Details

As with the solvent reaction coordinate, we evaluate the probability of forming configurations corresponding to the population coordinate TS in Eq. (3.36) by splitting it into two terms, where

$$\mathrm{P}\left(\mathbf{R}^{\ddagger}\right) = \frac{\int \{d\mathbf{R}_\alpha\}\, e^{-\frac{\beta}{N}H'_{MF}(\{\mathbf{R}_\alpha\})}\mathrm{Tr}\left[\Gamma_{\Delta\mathbb{P}=-1}\right]\delta\left(\overline{\mathbf{R}} - \mathbf{R}^{\ddagger}\right)}{\int \{d\mathbf{R}_\alpha\}\, e^{-\frac{\beta}{N}H'_{MF}(\{\mathbf{R}_\alpha\})}\mathrm{Tr}\left[\Gamma_{\Delta\mathbb{P}=-1}\right]} \tag{3.40}$$

and

$$\mathrm{P}\left(n^{\ddagger}|\mathbf{R}^{\ddagger}\right) = \frac{\int \{d\mathbf{R}_\alpha\}\, e^{-\frac{\beta}{N}H'_{MF}(\{\mathbf{R}_\alpha\})}\mathrm{Tr}\left[\Gamma_{\Delta\mathbb{P}=0}\right]\delta\left(\overline{\mathbf{R}} - \mathbf{R}^{\ddagger}\right)}{\int \{d\mathbf{R}_\alpha\}\, e^{-\frac{\beta}{N}H'_{MF}(\{\mathbf{R}_\alpha\})}\mathrm{Tr}\left[\Gamma_{\Delta\mathbb{P}=-1}\right]\delta\left(\overline{\mathbf{R}} - \mathbf{R}^{\ddagger}\right)}. \tag{3.41}$$

Eq. (3.40) is evaluated with the same techniques used for Eq. (3.17), but here we employ the weighting function

$$W_4 = e^{-\frac{\beta}{N}H'_{MF}-\frac{1}{2}k_c\left(\overline{\mathbf{R}}-\mathbf{R}_i\right)^2}\mathrm{Tr}\left[\Gamma_{\Delta\mathbb{P}=-1}\right], \tag{3.42}$$

with

$$\mathrm{Tr}\left[\Gamma_{\Delta\mathbb{P}=-1}\right] = \mathrm{Tr}\left[\prod_{\alpha=1}^{N}\left(\mathbf{M}(\mathbf{R}_\alpha)\mathbb{P}_1\right)\right]. \tag{3.43}$$

We evaluate Eq. (3.41) using an approach similar to Eq. (3.18), but in this case we only include kinked configurations with equal numbers of beads in each state while still accounting for any number of kink-pairs. As an example, consider a two-state system ($K = 2$) for simplicity. A particular electronic configuration $\{n_\alpha\} \equiv \{j, w, m\}$ is characterized by the number of beads in state 1, which we denote as j, the number of kink-pairs present, which we denote as w, and m, which represents the particular electronic configuration in the subset of configurations that have the same values of j and w. Each of these configurations represents a single term in the full Γ expression and is achieved by inserting the appropriate set of projection matrices between the $\mathbf{M}$ matrices:

$$\Gamma_{\{j,w,m\}} \equiv \Gamma_{\{n_\alpha\}} = \Gamma_{n_1,n_2,\ldots,n_N} = \prod_{\alpha=1}^{N}\left(\mathbf{M}(\mathbf{R}_\alpha)\mathbb{P}_{n_\alpha}\right), \tag{3.44}$$

where n_α represents the state onto which we project the α^{th} ring polymer bead.

Combinations for which half of the beads are in one state and half are in the other correspond to $j = N/2$, and the number of possible kink-pairs ranges from 1 to $N/2$. Values for m range from 1 to m_{tot}, where m_{tot} depends on the particular values of j and w. Thus, for a given nuclear configuration the exact thermal weight of kink-pair configurations with $j = N/2$ can be expressed as

$$\mathrm{Tr}\left[\Gamma_{\Delta\mathbb{P}=0}\right] = \mathrm{Tr}\left[\sum_{w=1}^{N/2}\sum_{m=1}^{m_{\text{tot}}}\Gamma_{\{N/2,w,m\}}\right]. \tag{3.45}$$

For a large number of ring polymer beads, we achieve a more efficient implementation of Eq. (3.45) by calculating $m_{\text{tot}}(j, w)$ at the beginning of the simulation and choosing a "representative configuration" $\{n_\alpha\} \equiv \{j = N/2, w\}'$ for every possible value of w. This allows us to evaluate $\text{Tr}\left[\Gamma_{\Delta\mathbb{P}=0}\right]$ at each MC step as a sum over representative combinations weighted by $m_{\text{tot}}(j, w)$:

$$\text{Tr}\left[\Gamma_{\Delta\mathbb{P}=0}\right] = \text{Tr}\left[\sum_{w=1}^{N/2} m_{\text{tot}}(N/2, w)\,\Gamma_{\{N/2,w\}'}\right], \tag{3.46}$$

which, on average, yields the same result as Eq. (3.45). In the weak coupling regime, sampling can also be limited to configurations with $w = 1$ that dominate the sum; however, in the present work we do not find it necessary to impose this limit on the number of kink-pairs.

Finally, initial configurations for the MF-RPMD simulation are generated by importance sampling using the weighting function

$$W_5 = e^{-\frac{\beta}{N}H'_{MF}}\text{Tr}\left[\Gamma_{\Delta\mathbb{P}=0}\right], \tag{3.47}$$

and we implement $\delta\left(\overline{\mathbf{R}} - \mathbf{R}^\ddagger\right)$ by shifting the nuclear COM to $\mathbf{R}^\ddagger$. Trajectories initially constrained to this TS distribution are evolved using the Hamiltonian in Eq. (3.6), and the initial velocity of the population coordinate along a trajectory is determined by computing the rate of change of $\Delta\mathbb{P}$ using a finite difference approximation at very short times. The average forward velocity computed using this technique is then multiplied by $\text{P}\left(\mathbf{R}^\ddagger, n^\ddagger\right)$ to obtain the TST rate estimate.

3.4.2 Model Systems

We test our population coordinate scheme using model systems like those in Section 3.3.2, but here we consider only the lowest electronic coupling value,

$\Delta = 6.69 \times 10^{-7}$ a.u., and explore a broader range of driving forces. Table 3.5 lists the new model parameters, and the diabats are plotted in Fig. 3.7.

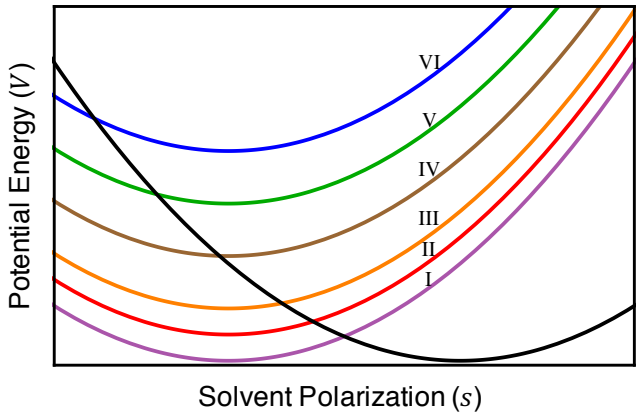

Figure 3.7: Electron transfer model systems with varying driving force studied using the population coordinate. Models I - VI correspond to the purple, red, orange, brown, green, and blue diabats, respectively. In each case, the colored curve represents the reactant state, and the black curve represents the product state. Note that the models describe all Marcus regimes of ET: Models I-III are in the normal regime, IV is activationless, and V-VI are in the inverted regime.

Table 3.5: Driving forces for the ET model systems studied using the population coordinate. All values are reported in atomic units.

Model	ϵ
I	0.0000
II	0.0296
III	0.0586
IV	0.1186
V	0.1776
VI	0.2366

3.4.3 Alternative Rate Theories

Since the model systems described in the previous section involve weakly-coupled states, we again compare our MF-RPMD rates to FGR. For reasons that

will become clear in the next section, we also compare to the Marcus theory (MT) rate for nonadiabatic ET involving a *classical* solvent [72]:

$$k_{\mathrm{MT}} = \frac{2\pi}{\hbar}|\Delta|^2 \sqrt{\frac{\beta}{4\pi\lambda}} e^{-\beta(\lambda-\epsilon)^2/4\lambda}, \tag{3.48}$$

where λ is the solvent reorganization energy, ϵ is the asymmetry between the reactant and product state energies at their respective minima, and Δ is the coupling between the reactant and product diabatic electronic states.

3.4.4 Results

MF-RPMD rates for the models provided in Section 3.4.2 are obtained by quantizing all degrees of freedom with $N = 32$ beads. For the k_{TST} calculation, we umbrella sample using 60 windows spaced evenly in the range $-6 < s < 0.5$ and constrained with a force constant $k_c = 200$ a.u. $\kappa_{\text{MF-RPMD}}(t)$ results are obtained by averaging over $30,000$ trajectories evolved using a fourth-order Adams-Bashforth-Moulton predictor-corrector integrator and a time step $dt = 0.1$ a.u., and numerical derivatives used to compute the initial $\Delta\mathbb{P}$ velocities are calculated by averaging $(\Delta\mathbb{P}(n \times dt) - \Delta\mathbb{P}(0)) / (n \times dt)$ for $n = 20, 30$, and 40.

Fig. 3.8 shows that rates obtained using the population coordinate, like the solvent coordinate, are quantitatively accurate, agreeing with FGR rates in the normal regime. Additionally, we are able to move past Model III to the activationless and inverted regimes (Models IV-VI), where the population coordinate remains a good reaction coordinate. The numerical values of our calculated rates, along with the TST rates, are reported in Table 3.6, and Fig. 3.9 shows $\kappa_{\text{MF-RPMD}}(t)$ for the different models; as in the previous case, $\kappa_{\text{MF-RPMD}}$ is approximately 1 for the symmetric model and decreases as the driving force increases.

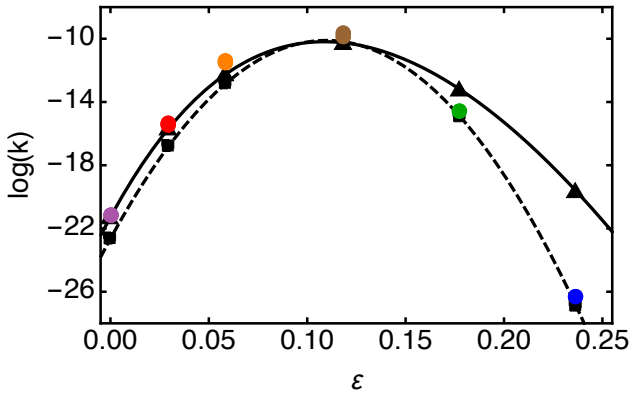

Figure 3.8: Electron transfer rate constants computed using the population reaction coordinate for a range of driving force values, ϵ, with constant coupling $\Delta = 6.69 \times 10^{-7}$ a.u. MF-RPMD results are shown in colored dots, FGR rate constants are shown in black triangles and a solid black line, and MT results are shown in black squares and a black dashed line. Both axes are reported in atomic units.

We note that in the inverted regime our results are qualitatively reasonable and capture the predicted turnover in rates, improving upon the original RPMD formulation which vastly overestimates rates for these models [42]. However, we do not find quantitative agreement with FGR but instead align more closely with Marcus theory. Recall that our definition of k_{TST} does not allow kinked configurations of the ring polymer to form except at solvent configurations corresponding to the point of degeneracy between the two diabats—this strict constraint prevents tunneling in the inverted regime that would otherwise lead to larger rates [27].

3.5 Summary

We showed in this chapter how one approach to formulating imaginary-time path integrals in state space leads to a method called mean field RPMD, which describes nuclear dynamics on a weighted average potential energy surface.

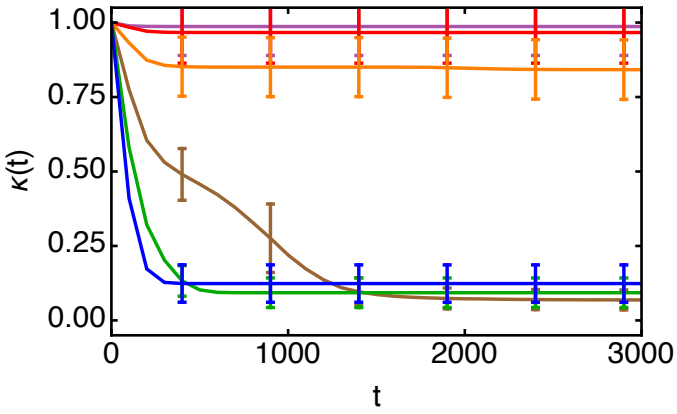

Figure 3.9: Plots of the dynamical recrossing term, $\kappa_{\text{MF-RPMD}}(t)$, computed using the population reaction coordinate as a function of time for Models I-VI (purple, red, orange, brown, green, and blue, respectively). Both axes are reported in atomic units.

Table 3.6: Electron transfer rate constants computed using the population coordinate for a range of driving forces, ϵ, with constant coupling $\Delta = 6.69\times10^{-7}$ a.u. From left to right, the four rightmost columns report the TST estimate to the rate constant, the full MF-RPMD rate constant, Fermi's golden rule values, and Marcus theory rate constants, respectively. The numbers in parentheses represent the statistical uncertainty in the last digit shown, and all values are reported in atomic units.

Model	ϵ	$\log(k_{\text{TST}})$	$\log(k_{\text{MF-RPMD}})$	$\log(k_{\text{FGR}})$	$\log(k_{\text{MT}})$
I	0.0000	-21.18(8)	-21.19(9)	-21.28	-22.65
II	0.0296	-15.34(4)	-15.36(6)	-15.66	-16.79
III	0.0586	-11.37(5)	-11.45(7)	-12.23	-12.83
IV	0.1186	-8.72(5)	-9.9(2)	-10.26	-10.19
V	0.1776	-13.50(5)	-14.5(2)	-13.20	-14.91
VI	0.2366	-25.44(7)	-26.3(2)	-19.63	-26.89

We then introduced a correction to the traditional solvent-based MF-RPMD rate equation that accounts for the probability of forming electronic transition states and which allows us to calculate accurate rate constants across the full range of electronic coupling strengths. Although calculating accurate nonadiabatic rate constants using MF-RPMD is an exciting feat, this scheme's inconsistent treatment of the transition state and reaction coordinate and its restriction to the normal regime of ET led us to introduce a new reaction coordinate based on

electronic state populations. The population coordinate distinguishes between reactants and products in all regimes of ET and allows us to achieve the desired turnover in the Marcus inverted regime; however, a restriction on kink formation outside of the diabatic crossing point prevented quantitative agreement with exact rates for models describing ET in the inverted regime. Note that although we tested our theories on systems undergoing single electron transfer, the state space path integral formulation described in this chapter is general for multi-electron systems and for systems involving more than two electronic states.

Moving forward, despite the rarity of the inverted regime, one may wish to correct the MF-RPMD rates for these models—Appendix A discusses one possible avenue towards achieving this goal. More interestingly, however, suppose we wish to move beyond rate theory and study a reaction such as a photochemical process that cannot be described by mean field dynamics. Doing so in the state space picture will require some way of representing electronic states using *continuous* variables that can be integrated in a classical MD simulation. The next chapter is devoted to discussing one such method and describing how we use it to simulate photochemistry.

CHAPTER 4

SIMULATING PHOTOCHEMISTRY WITH MAPPING VARIABLE RING POLYMER MOLECULAR DYNAMICS

Researchers have discovered numerous pathways for introducing explicit, continuous electronic state variables into the MF-RPMD framework that eliminate the need to average over electronic states. The KC-RPMD method, for example, employs a continuous collective variable that reports on the presence of kink-pairs, which, combined with a constraint on kink formation, has been shown to be highly accurate for rate calculations in all regimes of ET [27, 47]. Presently, however, this method remains limited to two-state systems and does not preserve the exact Boltzmann distribution. Unlike KC-RPMD, the nonadiabatic RPMD method developed by Richardson and coworkers, which represents discrete electronic states with classical harmonic oscillator variables, is not limited to two-state systems, but it also fails to preserve the thermal distribution [26]. In this work, we focus on an alternative approach, mapping variable RPMD, that also maps electronic states to classical phase space variables but manages to retain all the attractive features of the original RPMD formulation—favorable scaling in computational effort with system size, a consistent dynamic framework for electronic state transitions and nuclear dynamics, *and* dynamics that preserve detailed balance—while also remaining applicable to systems with more than two states [6].

In the method's inaugural paper, Ananth showed that MV-RPMD trajectories correctly capture nonadiabatic dynamics at equilibrium over a wide range of coupling strengths [6]. However, the method lacked two necessary features for simulating photo-initiated dynamics: 1) a reliable function that reports elec-

tronic state populations in time and 2) a way of constraining a system to a particular initial electronic state. In this chapter, we address these problems by deriving an exact expression for calculating electronic state populations in the MV-RPMD framework, and we use this expression to develop a simple and efficient protocol to initialize a simulation to a single electronic state. We then numerically demonstrate the accuracy of MV-RPMD trajectories in capturing electronic state dynamics for a series of model nonadiabatic systems with one or more avoided crossings [7].

4.1 Mapping Variable Ring Polymer Molecular Dynamics

Let us begin by reviewing the MV-RPMD formulation. Consider again the general Hamiltonian for a K-level system in the diabatic representation,

$$\hat{H} = \sum_{j=1}^{d} \frac{\hat{P}_j^2}{2M_j} + \sum_{n,m=1}^{K} |\psi_n\rangle V_{nm}(\hat{\mathbf{R}}) \langle\psi_m|, \tag{4.1}$$

where $\{|\psi_n\rangle\}$ represents the set of K discrete electronic states. Following the Meyer-Miller-Stock-Thoss (MMST) protocol [73, 74], we map the K electronic states to K singly excited oscillator (SEO) states,

$$|\psi_n\rangle\langle\psi_m| \rightarrow a_n^+ a_m \tag{4.2}$$

$$|\psi_n\rangle \rightarrow |0_1, \cdots, 1_n, \cdots, 0_K\rangle, \tag{4.3}$$

where a_n^+ and a_m are boson creation and annihilation operators that satisfy the commutation relation $[a_n^+, a_m] = \delta_{nm}$ and the SEO state, henceforth denoted $|n\rangle \equiv |0_1, \cdots, 1_n, \cdots, 0_K\rangle$, represents the direct product of K independent harmonic oscillators with $K-1$ in the ground state and the n^{th} oscillator in the first excited state. Note that SEO states represent a subspace in the full space of K harmonic oscillators.

We now introduce continuous position variables corresponding to the electronic states by discretizing the partition function using a representation of identity that preserves the mapping subspace [75],

$$\hat{\mathbb{1}} = \int d\mathbf{x} \int d\mathbf{R} \; |\mathbf{x}, \mathbf{R}\rangle\langle \mathbf{x}, \mathbf{R}| \; \hat{\mathbb{P}}, \tag{4.4}$$

where $\hat{\mathbb{P}} = \sum_n |n\rangle\langle n|$ represents projection onto the SEO basis, $\mathbf{R}$ corresponds to nuclear position, and the K-dimensional position vector $\mathbf{x}$ is associated with the electronic states. Inserting Eq. (4.4), evaluating nuclear kinetic energy terms, and multiplying by normalized Gaussian momentum integrals for the nuclear degrees of freedom, as in the previous chapters, we derive the following PI expression for the partition function:

$$\begin{aligned} Z \propto \lim_{N\to\infty} \int \{d\mathbf{x}_\alpha\} \int \{d\mathbf{R}_\alpha\} \int \{d\mathbf{P}_\alpha\} \prod_{\alpha=1}^{N} e^{-\frac{\beta}{N}\sum_{j=1}^{d}\left[\frac{P_{j,\alpha}^2}{2M_j} + \frac{M_j N^2}{2\beta^2\hbar^2}(R_{j,\alpha} - R_{j,\alpha+1})^2\right]} \\ \times \langle \mathbf{x}_\alpha | \hat{\mathbb{P}} e^{-\frac{\beta}{N}\mathbf{V}(\mathbf{R}_\alpha)} \hat{\mathbb{P}} | \mathbf{x}_{\alpha+1} \rangle, \end{aligned} \tag{4.5}$$

with $\mathbf{V}(\mathbf{R}_\alpha)$ representing the diabatic potential energy matrix and the proportionality sign indicating that pre-multiplicative constants have been omitted for simplicity.

For classical MD simulations, we must also introduce continuous momentum variables for electronic states, but doing so is not as straightforward as multiplying by normalized Gaussian integrals—this is because both electronic position and momentum must remain constrained to the mapping subspace. Instead, we harness the power of Wigner-Weyl transforms to represent the trace over a quantum operator $\hat{O}$ as an integral over classical phase space variables [76]:

$$\mathrm{Tr}\left[\hat{O}\right] = \frac{1}{(2\pi\hbar)^K} \int d\mathbf{x} \int d\mathbf{p} \;\; O(\mathbf{x}, \mathbf{p}), \tag{4.6}$$

where the Wigner function $O(\mathbf{x}, \mathbf{p})$ is defined as

$$O(\mathbf{x}, \mathbf{p}) = \int d\Delta\mathbf{x} \langle \mathbf{x} - \frac{\Delta\mathbf{x}}{2} | \hat{O} | \mathbf{x} + \frac{\Delta\mathbf{x}}{2} \rangle e^{i\mathbf{p}\cdot\Delta\mathbf{x}}. \tag{4.7}$$

To use Eqs. (4.6) and (4.7), we note that Z can be rewritten as a trace over the variable $\mathbf{x}_1$,

$$Z \propto \lim_{N\to\infty} \int \{d\mathbf{x}_\alpha\}_{2\to N} \int \{d\mathbf{R}_\alpha\} \int \{d\mathbf{P}_\alpha\} \, e^{-\frac{\beta}{N}\sum_{j=1}^{d}\sum_{\alpha=1}^{N}\left[\frac{P_{j,\alpha}^2}{2M_j} + \frac{M_j N^2}{2\beta^2\hbar^2}(R_{j,\alpha} - R_{j,\alpha+1})^2\right]} \mathrm{Tr}\left[\hat{O}\right]_1, \tag{4.8}$$

where the notation $\{d\mathbf{x}_\alpha\}_{2\to N}$ indicates integration over ring polymer beads 2 through N, $\mathrm{Tr}\,[\cdot]_1$ represents a trace over the first electronic position variable, and in this case

$$\hat{O} = \hat{\mathbb{P}} e^{-\frac{\beta}{N}\mathbf{V}(\mathbf{R}_1)} \hat{\mathbb{P}} |\mathbf{x}_2\rangle \cdots \langle \mathbf{x}_N | \hat{\mathbb{P}} e^{-\frac{\beta}{N}\mathbf{V}(\mathbf{R}_N)} \hat{\mathbb{P}}. \tag{4.9}$$

Substituting the definitions in Eqs. (4.6), (4.7), and (4.9) into Z, we find

$$\begin{aligned} Z \propto \lim_{N\to\infty} \int \{d\mathbf{x}_\alpha\} \int \{d\mathbf{R}_\alpha\} \int \{d\mathbf{P}_\alpha\} \int d\mathbf{p}_1 \int d\Delta\mathbf{x}_1 \, e^{-\frac{\beta}{N}\sum_{j=1}^{d}\sum_{\alpha=1}^{N}\left[\frac{P_{j,\alpha}^2}{2M_j} + \frac{M_j N^2}{2\beta^2\hbar^2}(R_{j,\alpha} - R_{j,\alpha+1})^2\right]} \\ \times \langle \mathbf{x}_1 - \frac{\Delta\mathbf{x}_1}{2} | \hat{\mathbb{P}} e^{-\frac{\beta}{N}\mathbf{V}(\mathbf{R}_1)} \hat{\mathbb{P}} | \mathbf{x}_2 \rangle \cdots \langle \mathbf{x}_N | \hat{\mathbb{P}} e^{-\frac{\beta}{N}\mathbf{V}(\mathbf{R}_N)} \hat{\mathbb{P}} | \mathbf{x}_1 + \frac{\Delta\mathbf{x}_1}{2} \rangle e^{i\mathbf{p}_1\cdot\Delta\mathbf{x}_1}. \end{aligned} \tag{4.10}$$

We can further rewrite the integral over $\mathbf{x}_2$ as a trace, replace the trace with a phase-space integral over the corresponding Wigner function, and repeat this procedure until electronic momentum variables have been introduced for all beads.

Electronic matrix elements in the resulting expression are evaluated using the SEO wavefunction,

$$\langle \mathbf{x} | n \rangle = \frac{\sqrt{2}}{\pi^{K/4}} \left[\mathbf{x}\right]_n e^{-\frac{1}{2}\mathbf{x}\cdot\mathbf{x}}, \tag{4.11}$$

where $[\cdot]_n$ indicates the n^{th} element of the enclosed vector, and Boltzmann matrix elements can be evaluated as in the previous chapter to give

$$\langle n_\alpha | e^{-\frac{\beta}{N}\mathbf{V}(\mathbf{R}_\alpha)} | n_{\alpha+1} \rangle \approx \left[\mathbf{M}(\mathbf{R}_\alpha)\right]_{n_\alpha n_{\alpha+1}}, \tag{4.12}$$

where again $\mathbf{M}$ has elements

$$[\mathbf{M}(\mathbf{R}_\alpha)]_{n_\alpha n_{\alpha+1}} = \begin{cases} e^{-\frac{\beta}{N} V_{n_\alpha n_\alpha}(\mathbf{R}_\alpha)} & n_\alpha = n_{\alpha+1} \\ -\frac{\beta}{N} V_{n_\alpha n_{\alpha+1}}(\mathbf{R}_\alpha)\, e^{-\frac{\beta}{N} V_{n_\alpha n_\alpha}(\mathbf{R}_\alpha)} & n_\alpha \neq n_{\alpha+1}. \end{cases} \tag{4.13}$$

Finally, analytically integrating over $\{\Delta\mathbf{x}_\alpha\}$ gives us a full phase space PI expression for the partition function:

$$Z \propto \lim_{N\to\infty} \int \{d\mathbf{x}_\alpha\} \int \{d\mathbf{p}_\alpha\} \int \{d\mathbf{R}_\alpha\} \int \{d\mathbf{P}_\alpha\}\, e^{-\frac{\beta}{N} H_{MV}(\{\mathbf{x}_\alpha\},\{\mathbf{p}_\alpha\},\{\mathbf{R}_\alpha\},\{\mathbf{P}_\alpha\})} \mathrm{sign}(\Theta)\,. \tag{4.14}$$

In Eq. (4.14), the variables $\mathbf{x}_\alpha$ and $\mathbf{p}_\alpha$ are continuous position and momentum vectors of length K that represent the K electronic states associated with the α^{th} ring polymer bead, and the nuclear positions and momenta of this bead are represented by the d-dimensional vectors $\mathbf{R}_\alpha$ and $\mathbf{P}_\alpha$, respectively. These variables interact through the classical Hamiltonian,

$$H_{MV} = \sum_{j=1}^{d} \sum_{\alpha=1}^{N} \left[\frac{P_{j,\alpha}^2}{2M_j} + \frac{M_j N^2}{2\beta^2\hbar^2} (R_{j,\alpha} - R_{j,\alpha+1})^2 \right] + \sum_{\alpha=1}^{N} \left[\frac{N}{\beta} (\mathbf{x}_\alpha \cdot \mathbf{x}_\alpha + \mathbf{p}_\alpha \cdot \mathbf{p}_\alpha) \right] - \frac{N}{\beta} \ln|\Theta|, \tag{4.15}$$

and together describe transitions between diabatic potential energy surfaces. In Eq. (4.15), $\Theta = \mathrm{Re}\,[\Gamma]$, and our new definition of Γ is

$$\Gamma = \mathrm{Tr}\left[\prod_{\alpha=1}^{N} \left((\mathbf{x}_\alpha + i\mathbf{p}_\alpha)(\mathbf{x}_\alpha - i\mathbf{p}_\alpha)^T - \frac{1}{2}\mathbb{1} \right) \mathbf{M}(\mathbf{R}_\alpha) \right], \tag{4.16}$$

with $\mathbb{1}$ representing the identity matrix. Note that Θ only includes the real portion of Γ because the Boltzmann distribution is real-valued, and the presence of the sign(Θ) term in Eq. (4.14) indicates Γ can be negative. Fortunately, unlike semiclassical methods that often suffer from numerical sign problems, the non-oscillatory structure of the quantum Boltzmann distribution in the formulation above has ensured that, in all cases tested thus far, numerical convergence with respect to bead number is achieved well before the average value of the sign function approaches zero.

Finally, real-time MV-RPMD thermal correlation functions are expressed as

$$\widetilde{C}_{AB}^{MV}(t) \approx \frac{\left\langle e^{-\frac{\beta}{N}H_{MV}}\text{sign}(\Theta)A_N(0)B_N(t)\right\rangle}{\left\langle e^{-\frac{\beta}{N}H_{MV}}\text{sign}(\Theta)\right\rangle}. \tag{4.17}$$

Initial distributions for these dynamics are best generated using PIMC importance sampling with respect to the weighting function $e^{-\frac{\beta}{N}H_{MV}}$—since the sign term is conserved by the classical MV-RPMD Hamiltonian, a single PIMD trajectory cannot sample the full space. As shown in Ref. 6, Eq. (4.17) offers a vast improvement over the analogous mean field expression for nuclear dynamics along weakly-coupled potential energy surfaces when A_N and B_N are functions of $\{\mathbf{R}_\alpha\}$. However, for photochemical reactions, we also wish to calculate dynamical correlations where A_N and B_N are functions of electronic variables and report on electronic state populations. The next section is devoted to deriving one such "population estimator" that makes this possible.

4.2 Population Estimators

In Section 3.2 (Eq. (3.10)), we presented a function that reports equilibrium electronic state populations in the mean field framework. A similar expression for the population of state n can be obtained in the mapping variable context [6],

$$\left\langle\hat{\mathbb{P}}_n\right\rangle = \frac{1}{Z}\text{Tr}[e^{-\beta\hat{H}}\hat{\mathbb{P}}_n] = \lim_{N\to\infty}\frac{\left\langle e^{-\frac{\beta}{N}H_{MV}}\text{sign}(\Theta)\frac{\text{Re}[\text{Tr}[\Gamma\mathbb{P}_n]]}{\text{Re}[\text{Tr}[\Gamma]]}\right\rangle}{\left\langle e^{-\frac{\beta}{N}H_{MV}}\text{sign}(\Theta)\right\rangle}, \tag{4.18}$$

which we achieve by tacking the projection operator $\hat{\mathbb{P}}_n$ onto $\hat{O}$ (Eq. (4.9)) in the mapping variable PI derivation. The term $\frac{\text{Re}[\text{Tr}[\Gamma\mathbb{P}_n]]}{\text{Re}[\text{Tr}[\Gamma]]}$ is often referred to as a "population estimator," and its ensemble average gives us the exact equilibrium population. This particular form of the population estimator, henceforth called the "Boltzmann estimator," is perhaps the most obvious, but it exhibits certain

features that make it less than ideal for tracking transitions between electronic states along the approximate MV-RPMD dynamics; namely, it is a function of not only electronic state variables but also nuclear position and temperature via the **M** matrices. This means that the population values it reports as a function of time could be unphysically influenced by these extraneous variables, and using this estimator to constrain initial populations in a simulation introduces an additional constraint on the initial nuclear distribution.

We wish instead to derive an estimator that depends only on electronic state variables. Consider the expression

$$\left\langle \hat{\mathbb{P}}_n \right\rangle \propto \lim_{N\to\infty} \frac{1}{Z} \int \{d\mathbf{x}_\alpha\} \int \{d\mathbf{R}_\alpha\} \int \{d\mathbf{P}_\alpha\} \prod_{\alpha=1}^{N} e^{-\frac{\beta}{N}\sum_{j=1}^{d}\left[\frac{P_{j,\alpha}^2}{2M_j}+\frac{M_j N^2}{2\beta^2\hbar^2}(R_{j,\alpha}-R_{j,\alpha+1})^2\right]} \times \langle \mathbf{x}_\alpha | \hat{\mathbb{P}} e^{-\frac{\beta}{N}\mathbf{V}(\mathbf{R}_\alpha)} \hat{\mathbb{P}} \hat{\mathbb{P}}_n | \mathbf{x}_{\alpha+1} \rangle, \tag{4.19}$$

which we find by PI discretizing the thermal quantum average electronic state population in the mapping variable framework. Rather than including $\hat{\mathbb{P}}_n$ with the other operators in the expression above, as we do when deriving the Boltzmann estimator, we recognize that the trace of a product of two operators is equal to the integral over phase-space variables of the product of their Wigner functions:

$$\mathrm{Tr}\left[\hat{A}\hat{B}\right] = \frac{1}{(2\pi\hbar)^K} \int d\mathbf{x} \int d\mathbf{p}\; A(\mathbf{x},\mathbf{p}) B(\mathbf{x},\mathbf{p}). \tag{4.20}$$

Thus, keeping the definition of $\hat{O}$ from Eq. (4.9), we rewrite Eq. (4.19) as

$$\left\langle \hat{\mathbb{P}}_n \right\rangle \propto \lim_{N\to\infty} \frac{1}{Z} \int \{d\mathbf{x}_\alpha\}_{2\to N} \int \{d\mathbf{R}_\alpha\} \int \{d\mathbf{P}_\alpha\}\, e^{-\frac{\beta}{N}\sum_{j=1}^{d}\sum_{\alpha=1}^{N}\left[\frac{P_{j,\alpha}^2}{2M_j}+\frac{M_j N^2}{2\beta^2\hbar^2}(R_{j,\alpha}-R_{j,\alpha+1})^2\right]} \times \mathrm{Tr}\left[\hat{O}\hat{\mathbb{P}}_n\right]_1, \tag{4.21}$$

which, using Eq. (4.20), becomes

$$\left\langle \hat{\mathbb{P}}_n \right\rangle \propto \lim_{N\to\infty} \frac{1}{Z} \int \{d\mathbf{x}_\alpha\} \int \{d\mathbf{R}_\alpha\} \int \{d\mathbf{P}_\alpha\} \int d\mathbf{p}_1 \; e^{-\frac{\beta}{N}\sum_{j=1}^{d}\sum_{\alpha=1}^{N}\left[\frac{P_{j,\alpha}^2}{2M_j} + \frac{M_j N^2}{2\beta^2\hbar^2}(R_{j,\alpha}-R_{j,\alpha+1})^2\right]} \times O(\mathbf{x}_1,\mathbf{p}_1)\mathcal{P}_n(\mathbf{x}_1,\mathbf{p}_1), \tag{4.22}$$

where the Wigner function for the projection operator is

$$\mathcal{P}_n(\mathbf{x}_1,\mathbf{p}_1) = 2^{K+1} e^{-\mathbf{x}_1\cdot\mathbf{x}_1 - \mathbf{p}_1\cdot\mathbf{p}_1}\left([\mathbf{x}_1]_n^2 + [\mathbf{p}_1]_n^2 - \frac{1}{2}\right). \tag{4.23}$$

Evaluation of $O(\mathbf{x}_1,\mathbf{p}_1)$ proceeds as before, eventually yielding the following expression for the average population of electronic state n:

$$\left\langle \hat{\mathbb{P}}_n \right\rangle = \lim_{N\to\infty} \frac{\left\langle e^{-\frac{\beta}{N}H_{MV}}\mathrm{sign}(\Theta)\,\mathcal{P}_n(\mathbf{x}_1,\mathbf{p}_1)\right\rangle}{\left\langle e^{-\frac{\beta}{N}H_{MV}}\mathrm{sign}(\Theta)\right\rangle}. \tag{4.24}$$

Finally, we note that the choice of bead 1 in Eq. (4.24) is arbitrary, and by cyclically relabeling beads we can define a bead-invariant population estimator that is an average of $\mathcal{P}_n$ over all beads:

$$\left\langle \hat{\mathbb{P}}_n \right\rangle = \lim_{N\to\infty} \frac{\left\langle e^{-\frac{\beta}{N}H_{MV}}\mathrm{sign}(\Theta)\,\bar{\mathcal{P}}_n\right\rangle}{\left\langle e^{-\frac{\beta}{N}H_{MV}}\mathrm{sign}(\Theta)\right\rangle}, \tag{4.25}$$

where the "Wigner estimator,"

$$\bar{\mathcal{P}}_n = \frac{1}{N}\sum_{\alpha=1}^{N}\left[2^{K+1} e^{-\mathbf{x}_\alpha\cdot\mathbf{x}_\alpha - \mathbf{p}_\alpha\cdot\mathbf{p}_\alpha}\left([\mathbf{x}_\alpha]_n^2 + [\mathbf{p}_\alpha]_n^2 - \frac{1}{2}\right)\right], \tag{4.26}$$

is a pure function of electronic state variables.[1] Not surprisingly, Eq. (4.26) is similar to population functions used in semiclassical methods that employ MMST mapping, but here it has been derived exactly in the MV-RPMD framework.

[1] A similar MV-RPMD population estimator that is also purely a function of electronic state variables can be derived by expressing the projection operator in terms of ladder operators, $\hat{\mathbb{P}}_n = a_n^+ a_n$. See Ref. 77 for details.

4.3 Constraining Electronic State Populations

In addition to a reliable population estimator, simulations of many interesting physical processes, especially photo-initiated ones, require a system to be initialized to a particular electronic state. In general, to study electronic state dynamics from an initial non-equilibrium state, $|\psi_i\rangle$, one solves the quantum correlation function

$$\left\langle \hat{\mathbb{P}}_n(t) \right\rangle = \frac{\mathrm{Tr}\left[|\psi_i\rangle\langle\psi_i|\, e^{i\hat{H}t/\hbar}\, \hat{\mathbb{P}}_n\, e^{-i\hat{H}t/\hbar} \right]}{\mathrm{Tr}\left[|\psi_i\rangle\langle\psi_i| \right]}. \tag{4.27}$$

Using the new Wigner population estimator, the MV-RPMD approximation to Eq. (4.27) becomes

$$\left\langle \hat{\mathbb{P}}_n(t) \right\rangle \approx \frac{\left\langle f\left(\{\mathbf{R}_\alpha, \mathbf{P}_\alpha\}\right) \prod_{\alpha=1}^{N} \prod_{k=1}^{K} \delta(\mathcal{P}_k(\alpha) - a_k)\, \bar{\mathcal{P}}_n(t) \right\rangle}{\left\langle f\left(\{\mathbf{R}_\alpha, \mathbf{P}_\alpha\}\right) \prod_{\alpha=1}^{N} \prod_{k=1}^{K} \delta(\mathcal{P}_k(\alpha) - a_k) \right\rangle}, \tag{4.28}$$

where the Boltzmann factor has been replaced with separate functions, f and δ, that determine the initial nuclear distribution and electronic state populations, respectively. The initial nuclear distribution is generated using PIMC importance sampling on the weighting function f, which is system-dependent and will be discussed later in the context of specific model systems. Constraints on the initial electronic state populations are represented by the delta functions in Eq. (4.28), where a_k takes values 1 or 0 based on the initial occupation of the k^{th} electronic state.

Numerous approaches to implementing an electronic state constraint can be considered. However, we find only one, similar in spirit to the focusing approximation in the context of semiclassical simulations [78], that is stringent enough to ensure the system starts in the desired electronic state: we set each term in the summation in Eq. (4.26) to 1 if state n is fully occupied and to 0 if it is unoc-

cupied, solving the single-bead equation

$$\mathcal{P}_n(\alpha) \equiv 2^{K+1} e^{-\mathbf{x}_\alpha \cdot \mathbf{x}_\alpha - \mathbf{p}_\alpha \cdot \mathbf{p}_\alpha} \left([\mathbf{x}_\alpha]_n^2 + [\mathbf{p}_\alpha]_n^2 - \frac{1}{2} \right) = a_n = \begin{cases} 1 \\ \\ 0 \end{cases} \tag{4.29}$$

for $[\mathbf{x}_\alpha]_n^2 + [\mathbf{p}_\alpha]_n^2 \equiv r^2$. For unoccupied states, the solution is $r_0 = \sqrt{0.5}$, whereas for the single fully occupied state there will be two solutions whose values depend on the total number of electronic states in the system. In practice, we use only the larger of these two solutions, henceforth called r_1, because the smaller radius proves numerically unstable (reasons for this remain unclear and will be the focus of future work). Thus, to initialize an MV-RPMD simulation such that electronic state n is occupied, electronic variables $[\mathbf{x}_\alpha]_n$ and $[\mathbf{p}_\alpha]_n$ for each bead α are sampled on a circle of radius r_1 in phase space, while $[\mathbf{x}_\alpha]_m$ and $[\mathbf{p}_\alpha]_m$ for unoccupied states ($m \neq n$) are sampled on circles of radius r_0.

MV-RPMD trajectories released from such a constrained distribution move according to the Hamiltonian in Eq. (4.15). Because of the presence of β throughout this Hamiltonian, we require a fictitious temperature for these dynamics. Since temperature provides an indirect measure of the energy of a system, we choose this temperature to match the total initial energy, E, of the constrained system using the relationship $k_B T = E$. Bead convergence is then achieved by converging the *equilibrium* average energy calculated at this fictitious temperature using PIMC.

4.4 Two-State Transmission and Reflection

We first demonstrate use of the Wigner population estimator and initialization technique in the context of three one-dimensional model systems commonly

used to benchmark nonadiabatic dynamics methods [19]. The models describe wavepacket transmission and reflection on two coupled potential energy surfaces.

4.4.1 Model Systems

Model I involves a simple avoided crossing. In the diabatic representation, the potential energy curves and off-diagonal coupling functions are

$$\begin{aligned} V_{11}(R) &= \begin{cases} -0.01\left[1 - e^{1.6R}\right] + 0.01 & R < 0, \\ 0.01\left[1 - e^{-1.6R}\right] + 0.01 & R \geq 0 \end{cases} \\ V_{22}(R) &= -V_{11}(R), \quad \text{and} \\ V_{12}(R) &= V_{21}(R) = 0.005\, e^{-R^2}. \end{aligned} \tag{4.30}$$

Model II involves two avoided crossings with diabatic potential energy functions

$$\begin{aligned} V_{11}(R) &= 0, \\ V_{22}(R) &= -0.1\, e^{-0.28R^2} + 0.05, \quad \text{and} \\ V_{12}(R) &= V_{21}(R) = 0.015\, e^{-0.06R^2}, \end{aligned} \tag{4.31}$$

and Model III describes an extended region of coupling with diabatic potential energy functions

$$\begin{aligned} V_{11}(R) &= 0, \\ V_{22}(R) &= 0.0012, \quad \text{and} \\ V_{12}(R) &= V_{21}(R) = \begin{cases} 0.1\, e^{0.9R} & R < 0 \\ 0.1\left[2 - e^{-0.9R}\right] & R \geq 0. \end{cases} \end{aligned} \tag{4.32}$$

The potential curves and off-diagonal couplings are plotted in the left panel of Fig. 4.1 alongside our results.

For each of these models, the exact quantum picture describes an initial Gaussian wavepacket, $\psi(R) = e^{iP_0R}e^{-(R-R_0)^2/\sigma^2}$, for a particle of mass $M = 2,000$ a.u. The wavepacket initially occupies the lower-energy diabatic state, V_{11}, with a forward momentum distribution centered at P_0 and a nuclear position distribution centered at R_0 with width $\sigma = \frac{20}{P_0}$. To ensure our results are not fortuitously good, we test three different values of P_0 for each model (panels A, B, and C in Fig. 4.1); the kinetic energies associated with these values are indicated with arrows in the left panel of Fig. 4.1, and P_0 and R_0 are reported in Table 4.1.

Table 4.1: Initial position and momentum parameters for the Gaussian wavepackets in the two-state models. "Panel" refers to the corresponding column of results in Fig. 4.1. All values are reported in atomic units.

Model	Panel	P_0	R_0
I	A	6.3	-5
	B	8.9	-5
	C	10	-5
II	A	10	-7
	B	14.1	-7
	C	16	-7
III	A	1.6	-7
	B	2.2	-7
	C	4	-7

4.4.2 Dynamics Simulations

We ensure that the nuclear phase space distribution for each bead in MV-RPMD matches the corresponding quantum wavepacket probability distribution by us-

ing the sampling function

$$f\left(\{R_\alpha, P_\alpha\}\right) = \prod_{\alpha=1}^{N} e^{(R_\alpha - R_0)^2/\sigma^2} e^{(P_\alpha - P_0)^2\sigma^2/4}, \tag{4.33}$$

and the system is constrained to electronic state 1 by sampling electronic variables on circles of radius $r_0 = \sqrt{0.5}$ and $r_1 \approx 1.398$ (the solution to Eq. (4.29) for occupied states when $K = 2$). MV-RPMD trajectories released from such a constrained distribution are evolved using a fourth-order Adams-Bashforth-Moulton predictor-corrector integrator, and the temperature used for these dynamics is calculated from the initial energy, which in these systems simply corresponds to the kinetic energy, $\frac{P_0^2}{2M}$, since the lower potential surface is shifted to zero. Temperatures for the different models are reported in Table 4.2, along with the number of beads and trajectories required to converge our simulations to second decimal place as well as the timesteps required to conserve energy. For comparison, exact quantum dynamics results are obtained using the discrete variable representation (DVR) grid method [79]; parameters for these simulations are also reported in Table 4.2.

Table 4.2: Parameters for the MV-RPMD and DVR simulations. Unless otherwise specified, all values are reported in atomic units.

		MV-RPMD				DVR	
Model	Panel	N	T (K)	Trajectories	dt	Grid Range	Grid Spacing
I	A	3	3133	7200	0.1	$-15 < R < 15$	0.05
	B	3	6253	2400	0.1	$-15 < R < 15$	0.05
	C	3	7894	1920	0.1	$-15 < R < 15$	0.05
II	A	3	7894	2400	0.1	$-15 < R < 15$	0.05
	B	3	15695	1920	0.1	$-15 < R < 15$	0.05
	C	3	20210	1920	0.1	$-15 < R < 15$	0.05
III	A	8	202	38,400	0.005	$-30 < R < 30$	0.05
	B	8	382	21,600	0.005	$-30 < R < 30$	0.05
	C	6	1263	19,200	0.005	$-30 < R < 30$	0.05

As shown in Fig. 4.1, the circle constraint on electronic variables ensures that the mapping variable ring polymers fully populate the lower energy elec-

tronic state (red curve) at time zero for each of the models. As the simulation progresses, electronic population transfers between the two diabatic states, and we see that the MV-RPMD populations calculated using the Wigner estimator match the exact DVR results quite well, particularly at short times where we expect our approximate dynamics to be most accurate. We also note that our MV-RPMD results compare favorably with the transmission-reflection coefficients calculated using the popular surface hopping and surface hopping with decoherence methods in Ref. 80.

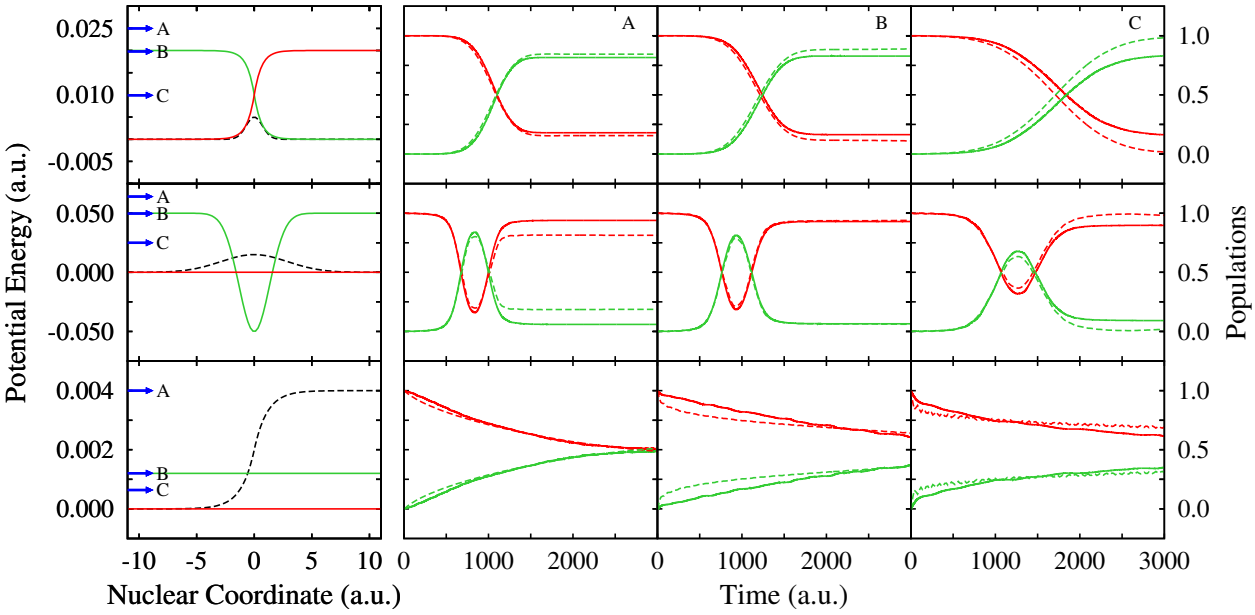

Figure 4.1: Diabatic potential energy functions and real-time electronic state populations for Models I, II, and III (top, middle, and bottom rows, respectively). The first column shows potential curves with solid colored lines and coupling functions with black dashed lines (the coupling function for Model III is scaled by 0.02 for clarity). Kinetic energies associated with the three values of P_0 tested for each model are indicated with blue arrows and are labeled to correspond to results in panels A, B, and C. MV-RPMD results in each panel are shown with solid lines, exact quantum results are shown with dashed lines, and lines are colored to match the diabats in the first column.

4.5 Three-State Photodissociation

We now turn to a more challenging set of models: three-state, single-mode systems parametrized to describe photodissocation [81]. The dimensionality of these systems is low enough that we can still compare to exact DVR calculations while also gaining an understanding of how well our method will perform for more complex systems like those in organic photovoltaics.

4.5.1 Model Systems

The physical picture in each model involves an initial occupied excited electronic state generated by optical excitation from a harmonic ground state using a femtosecond laser pulse. Assuming Franck-Condon excitation, the initial non-equilibrium state, $|\psi_i\rangle$, is a ground state harmonic oscillator wavefunction centered at R_0 with a population of 1 in excited electronic state $|1\rangle$. After photoexcitation, the sub-100 fs dynamics of the electronic state populations are assumed to evolve on a manifold of three coupled excited state surfaces, allowing us to ignore the ground state contribution to these dynamics.

The diagonal elements of the diabatic potential energy matrix for the excited state manifold are Morse potentials of the form

$$V_i = De_i(1 - e^{-\beta_i(R-Re_i)})^2 + c_i, \tag{4.34}$$

and the off-diagonal couplings are Gaussian functions centered at the crossing points R_{ij}:

$$V_{ij} = A_{ij}e^{-a_{ij}(R-R_{ij})^2}. \tag{4.35}$$

Parameters for these functions are reported in Table 4.3, and the potential curves and couplings are plotted in the left panel of Fig. 4.3, alongside the dynamics results. For all three models, the nuclear mass M is 20,000 a.u., and the frequency ω of the harmonic ground state potential is 0.005 a.u.

Table 4.3: Potential energy parameters for the three-state models describing photodissociation. All parameters are reported in atomic units.

	Model IV			Model V			Model VI		
i	1	2	3	1	2	3	1	2	3
De_i	0.02	0.02	0.003	0.02	0.01	0.003	0.003	0.004	0.003
β_i	0.4	0.65	0.65	0.65	0.4	0.65	0.65	0.6	0.65
Re_i	4	4.5	6	4.5	4	4.4	5	4	6
c_i	0.02	0	0.02	0	0.01	0.02	0	0.01	0.006
ij	12	13	23	12	13	23	12	13	23
A_{ij}	0.005	0.005	0	0.005	0.005	0	0.002	0	0.002
R_{ij}	3.4	4.97	0	3.66	3.34	0	3.4	0	4.8
a_{ij}	32	32	0	32	32	0	16	0	16

4.5.2 Equilibrium Simulation

Before considering dynamics, we demonstrate the accuracy of the Wigner estimator at equilibrium using Model IV. (For this simulation, we add an infinite wall at $R = 10$ a.u. to ensure all states are bounded.) The thermal Boltzmann distribution is generated using standard PIMC techniques, where the temperature is the same one we will use in the next section for dynamics, $T = 15288$ K, which is derived from the total energy of the initial excited system. The equilibrium properties we consider here are the state-specific nuclear probability distributions of the three excited electronic states, which are calculated in the mapping variable PI framework using the expression [75]

$$\mathrm{P}(n,R) = \frac{\left\langle e^{-\frac{\beta}{N}H_{MV}}\ \mathrm{sign}(\Theta)\ \delta(R-R_i)\ \bar{\mathcal{P}}_n \right\rangle}{\left\langle e^{-\frac{\beta}{N}H_{MV}}\ \mathrm{sign}(\Theta) \right\rangle}. \tag{4.36}$$

As shown in Fig.4.2, probabilities obtained using the Wigner estimator are indistinguishable from exact quantum results calculated using the DVR method.

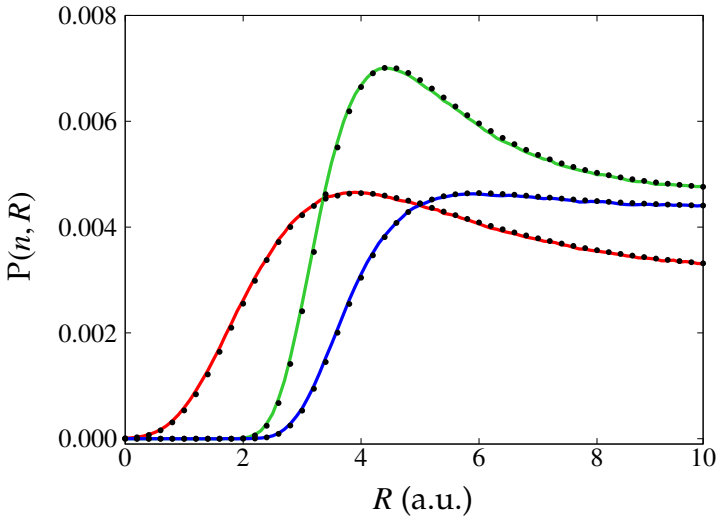

Figure 4.2: State-specific nuclear probability distributions for Model IV. Probabilities for states 1, 2, and 3 are shown in red, green, and blue, respectively. Wigner estimator results are displayed as lines and were converged using 3 ring polymer beads and 5×10^8 MC points (error bars are roughly the width of the lines). DVR results are shown in black dots and were converged using a grid range of R = 0 to 10 a.u. and a grid spacing of 0.05 a.u.

4.5.3 Dynamics Simulations

Turning now to the dynamics simulations, we generate the initial Franck-Condon nuclear distribution by PIMC sampling on the ground state Hamiltonian for a harmonic oscillator using the sampling function $f(\{R_\alpha, P_\alpha\}) = e^{-\frac{\beta'}{N} H'_N}$, where

$$H'_N = \sum_{\alpha=1}^{N} \left[\frac{P_\alpha^2}{2M} + \frac{MN^2}{2\beta'^2\hbar^2}(R_\alpha - R_{\alpha+1})^2 + \frac{1}{2}M\omega^2(R_\alpha - R_0)^2 \right] \tag{4.37}$$

and β' indicates that sampling is performed at 300 K. Electronic variables are sampled on circles of radius $r_0 = \sqrt{0.5}$ and $r_1 \approx 1.559$ (the solution to Eq. (4.29) for occupied states when $K = 3$). MV-RPMD trajectories released from this constrained distribution are evolved using a fourth-order Adams-Bashforth-Moulton predictor-corrector integrator and a timestep $dt = 0.1$ a.u. The fictitious temperature used for these dynamics is calculated from the initial energy, which for these models is the ZPE of the ground state plus the potential energy gap between the lowest *excited* state and the initial occupied excited state at R_0. (Since the Hamiltonian used for dynamics is not aware of the ground state, we do not need to account for the gap between the ground and lowest excited states when calculating the temperature.) These temperatures, along with other MV-RPMD simulation parameters, are reported in Table 4.4.

Table 4.4: Simulation parameters for the MV-RPMD, DVR, and LSC-IVR calculations. Unless otherwise specified, all values are reported in atomic units.

		MV-RPMD			DVR		LSC-IVR
Model	R_0	N	T (K)	Trajectories	Grid Range	Grid Spacing	Trajectories
IV	2.1	3	15288	1200	$0 < R < 20$	0.05	144,000
V	3.3	3	9605	900	$0 < R < 20$	0.05	28,800
VI	2.9	3	8843	720	$0 < R < 20$	0.05	28,800

For comparison, exact quantum dynamics results are obtained using the DVR grid method with an initial state $|\psi_i\rangle = e^{-\frac{M\omega}{2}(R-R_0)^2}|1\rangle\langle 1|$. Parameters for these simulations are reported in Table 4.4. We also compare our results to those obtained using the linearized semiclassical initial value representation (LSC-IVR) [21, 81], a method that also employs a consistent dynamic framework for nuclear and electronic state dynamics and neglects nuclear quantum coherence effects. Our implementation follows Ref. 81 and employs an initial nuclear coherent state of width $\gamma = M\omega$. Table 4.4 shows the number of trajectories needed for numerical convergence in the LSC-IVR simulations.

MV-RPMD, DVR, and LSC-IVR results are shown in the middle and right columns of Fig. 4.3. For all three models, MV-RPMD simulation results match the exact results at short times very well. Model IV involves an avoided crossing at longer times and a likely contribution from nuclear quantum coherence effects [81], making it the most challenging for our model dynamics to describe accurately. Models V and VI are better suited to the MV-RPMD approach, with both avoided crossings being accessible at shorter times, as evidenced by the significantly improved agreement with exact quantum results. Fig. 4.3 also shows that MV-RPMD performs significantly better than LSC-IVR for all three models. Because MV-RPMD trajectories remain constrained to the mapping subspace, populations obtained by averaging over the trajectory ensemble are never negative or greater than 1; in contrast, LSC-IVR's failure to obey detailed balance gives rise to unphysical population values. In Appendix B, we also provide MV-RPMD results in the $N = 1$ limit for these models as well as the ones studied in Section 4.4.

4.5.4 Summary

In this chapter, we reviewed the mapping variable ring polymer molecular dynamics method, an extension of the original RPMD approach that represents discrete electronic states using continuous position and momentum variables. Like mean field RPMD discussed in the previous chapter, the state space representation makes the MV-RPMD method applicable to multi-electron systems, but here we saw that the continuous electronic variables allow us to move from a mean field picture to dynamics that transition between discrete energy surfaces. We derived and tested a new electronic state population estimator in the MV-

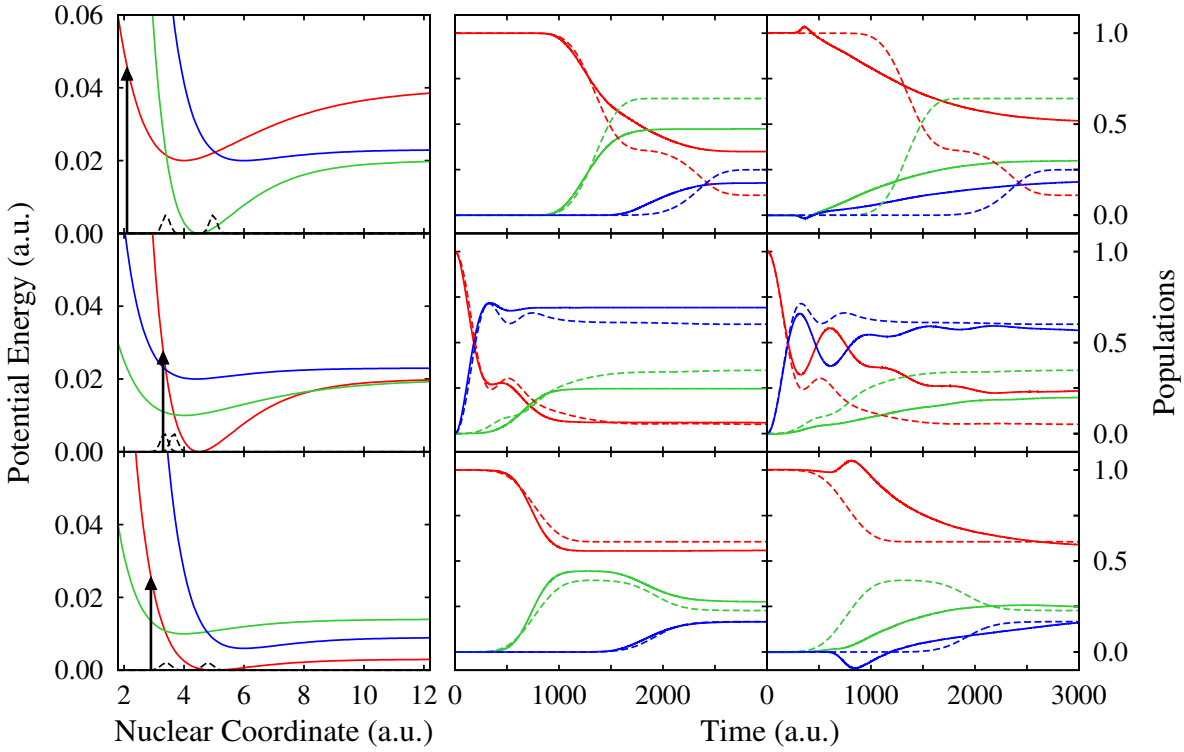

Figure 4.3: Diabatic potential energy curves and real-time electronic state populations for Models IV, V, and VI (top, middle, and bottom rows, respectively). The left column shows potential curves with solid lines and coupling functions with dashed lines; the center of the initial nuclear wavefunction constrained to excited state 1 is indicated by a black arrow. The middle column shows MV-RPMD results, and the right column shows LSC-IVR results, both with solid lines; in each of these columns we compare to exact DVR results, shown in dashed lines. In all cases, lines are colored to match the diabats in the left column.

RPMD framework that is purely a function of electronic state variables, and this estimator steered us naturally towards an efficient sampling scheme to generate MV-RPMD distributions corresponding to initial photo-excited electronic states. The numerical accuracy of the MV-RPMD results for all six models tested here makes it clear that the Wigner estimator is a good electronic state population estimator and, in combination with the initialization protocol, can accurately describe photo-induced electronic state dynamics.

CHAPTER 5

CONCLUSION

The primary focus of this dissertation has been the development of accurate and efficient methods for simulating quantum mechanical reactions in condensed-phase systems. We began with a review of the imaginary-time path integral formulation of quantum mechanics, an exact approach for calculating quantum statistical averages using classical mechanical techniques. We then discussed one real-time extension of the PI formulation, a method called ring polymer molecular dynamics that exclusively employs classical trajectories to approximate the quantum Kubo-transformed thermal correlation function. We argued that the lack of nuclear quantum coherence effects in RPMD is permissible, since our target applications are condensed-phase reactions; however, the method's limitation to single-electron processes—a by-product of the distinguishable-particle representation—makes it inapplicable to many reactions of interest, including photochemical dynamics.

RPMD's near-linear scaling, consistent dynamic framework, and ability to preserve the thermal distribution led us to explore extensions of the method for multi-electron systems. Chapter 3 focused on one such extension, mean field ring polymer molecular dynamics, that avoids the single-electron problem by reformulating RPMD in state space. Because this method lacks explicit electronic state variables and, therefore, propagates nuclear dynamics on a mean potential energy surface, it has failed to describe accurate nonadiabatic dynamics in previous applications. Here, however, we showed how the *implicit* electronic state information can be used to modify the standard MF-RPMD rate equation to account for the penalty of forming electronic transition states. This

new implementation allowed us to calculate accurate rate constants across the full range of electronic coupling strengths in model electron transfer systems.

More specifically, we reformulated the MF-RPMD rate equation using two different approaches. First, we considered the traditional solvent reaction coordinate that describes electron transfer progress in terms of the collective solvent polarization; we re-weighted the rate calculated using this coordinate by the probability of forming ring polymer kink-pairs, which represent electronic transition states in the MF-RPMD picture. This scheme yielded accurate rate constants in the weak and strong limits of electronic state coupling throughout the normal regime of electron transfer. For a more rigorous approach, we introduced a new reaction coordinate defined as the difference in the ring polymer bead populations of the electronic states. This approach not only yielded accurate rate constants in the nonadiabatic limit but also captured the turnover in rates in the Marcus inverted regime, a feat the original RPMD method fails to achieve. However, because MF-RPMD overestimates kink probabilities outside the diabatic curve intersection, we imposed a stringent constraint that restricts kink formation to configurations where the solvent ring polymer center of mass is positioned at the diabatic crossing point. This constraint prevents tunneling in the inverted regime and resulted in rates that agree quantitatively with Marcus theory for a classical solvent, rather than with golden rule for a quantum solvent.

Appendix A describes one possible route to correcting the MF-RPMD rates in the inverted regime. Additionally, because the models we tested in Chapter 3 involve intermediate coupling between the solvent and bath degrees of freedom, recent efforts have focused on testing MF-RPMD in the strong friction

(i.e. Zusman) regime. Our findings suggest the method is also accurate for these models [82]. Moving forward, we are now equipped with a reliable and scalable method for calculating reaction rate constants in a wide range of systems. Not only does the state space representation permit us to tackle multi-electron problems, but in many cases this representation is simply more convenient for single-electron reactions. Our research group is particularly interested in using MF-RPMD to compare the efficiencies of different chemical systems for technologies like dye-sensitized solar cells.

Despite the success of our MF-RPMD rate scheme, the method cannot be used to study excited electronic state dynamics. Thus, in Chapter 4 we presented mapping variable RPMD, a method developed in our research group which maps discrete electronic states to continuous phase space variables that can be used explicitly in classical MD simulations. MV-RPMD was originally intended for studying photochemical reactions but lacked the necessary tools to do so. To address this problem, we derived a function of the electronic state variables for tracking electronic state transitions in time, and we used this function to generate a protocol for constraining initial electronic state populations. As shown in Sections 4.4.2 and 4.5.3, MV-RPMD with the new population estimator and constraint protocol accurately models electronic state transmission/reflection and photodissociation in two- and three-state systems.

More recent work from our group has shown how a similar constraint on electronic state variables to *transition state* configurations allows us to study the mechanisms of proton-coupled electron transfer in system-bath models [83]. Future efforts will focus on ensuring the scheme presented here is just as accurate in higher-dimensional systems, particularly with regards to the nuclear degrees

of freedom. If this proves to be true, we wish to use the method to study the mechanisms of reactions important for solar energy harvesting, such as singlet fission in organic photovoltaics. A deeper understanding of these types of reactions will guide the design of improved materials for sustainable energy technologies.

APPENDIX A

CORRECTING MEAN FIELD RING POLYMER MOLECULAR DYNAMICS RATES IN THE INVERTED REGIME

When we introduced a scheme for calculating MF-RPMD rates using the population coordinate in Chapter 3, we added a stringent constraint that prevents kink formation except for configurations where the solvent ring polymer COM is positioned at the intersection of the reactant and product diabatic states. This constraint allows us to avoid a well-known problem with the RPMD method where transitions between potential wells in the inverted regime occur with unphysically large probabilities. However, such a tight constraint prevents tunneling and effectively forces the solvent ring polymer to behave more classically. As a result, rate constants calculated using our MF-RPMD approach in the inverted regime agree with Marcus theory, rather than FGR. Here we propose one possible pathway for loosening the constraint on kink formation in order to allow for tunneling.

We start with an expression for the full MF-RPMD rate constant that has no constraint on kink formation:

$$k = \frac{\int \{d\mathbf{R}_\alpha\} \int \{d\mathbf{P}_\alpha\}\, e^{-\frac{\beta}{N} H''_{MF}} \mathrm{Tr}\left[\Gamma_{\Delta\mathbb{P}=0}\right] \Delta\dot{\mathbb{P}}_0 h\left(\Delta\mathbb{P}_t\right)}{\int \{d\mathbf{R}_\alpha\} \int \{d\mathbf{P}_\alpha\}\, e^{-\frac{\beta}{N} H''_{MF}} \mathrm{Tr}\left[\Gamma_{\Delta\mathbb{P}=-1}\right]}, \tag{A.1}$$

where

$$H''_{MF} = \sum_{j=1}^{d} \sum_{\alpha=1}^{N} \left[\frac{P_{j,\alpha}^2}{2M_j} + \frac{M_j N^2}{2\beta^2\hbar^2} (R_{j,\alpha} - R_{j,\alpha+1})^2 \right]. \tag{A.2}$$

As in Section 3.4.1, $\mathrm{Tr}\left[\Gamma_{\Delta\mathbb{P}=0}\right]$ represents electronic configurations for which the difference in the bead populations of the two states is zero, $\mathrm{Tr}\left[\Gamma_{\Delta\mathbb{P}=-1}\right]$ refers to electronic configurations with all beads in the reactant state, and for the velocity and Heaviside terms we use the definition of $\Delta\mathbb{P}$ provided in Eq. (3.39). Fol-

lowing the Bennett-Chandler protocol, we factor the rate constant into a purely statistical term and a time-dependent recrossing factor,

$$k = k'_{\text{TST}} \times \kappa'_{\text{MF-RPMD}}(t) = \frac{\int \{d\mathbf{R}_\alpha\} \int \{d\mathbf{P}_\alpha\}\, e^{-\frac{\beta}{N} H''_{MF}} \text{Tr}\left[\Gamma_{\Delta\mathbb{P}=0}\right]}{\int \{d\mathbf{R}_\alpha\} \int \{d\mathbf{P}_\alpha\}\, e^{-\frac{\beta}{N} H''_{MF}} \text{Tr}\left[\Gamma_{\Delta\mathbb{P}=-1}\right]} \times \frac{\int \{d\mathbf{R}_\alpha\} \int \{d\mathbf{P}_\alpha\}\, e^{-\frac{\beta}{N} H''_{MF}} \text{Tr}\left[\Gamma_{\Delta\mathbb{P}=0}\right] \Delta\dot{\mathbb{P}}_0 h\left(\Delta\mathbb{P}_t\right)}{\int \{d\mathbf{R}_\alpha\} \int \{d\mathbf{P}_\alpha\}\, e^{-\frac{\beta}{N} H''_{MF}} \text{Tr}\left[\Gamma_{\Delta\mathbb{P}=0}\right]}, \tag{A.3}$$

where the first term on the righthand side of Eq. (A.3), k'_{TST}, represents the probability of kinked configurations for which $\Delta\mathbb{P} = 0$, compared to the probability of reactant state configurations. The second term, $\kappa'_{\text{MF-RPMD}}(t)$, represents the average initial velocity of trajectories that form product after reaching the transition state. Without a constraint on kink formation, these terms overestimate the probability of kinks outside the diabatic crossing point because $\text{Tr}\left[\Gamma_{\Delta\mathbb{P}=0}\right] > \text{Tr}\left[\Gamma_{\Delta\mathbb{P}=-1}\right]$ for solvent configurations where $V_{22}(R) < V_{11}(R)$.

To correct this problem, we recognize that, for a given value of the solvent coordinate, the ratio $\text{Tr}\left[\Gamma_{\Delta\mathbb{P}=0}\right]/\text{Tr}\left[\Gamma\right]$ properly accounts for the probability of $\Delta\mathbb{P} = 0$, since Γ represents a sum over *all* electronic configurations and is dominated by Boltzmann factors corresponding to the lower-energy state. We incorporate this ratio into k'_{TST} by multiplying and dividing by Γ in the numerator:

$$k'_{\text{TST}} = \frac{\int \{d\mathbf{R}_\alpha\} \int \{d\mathbf{P}_\alpha\}\, e^{-\frac{\beta}{N} H''_{MF}} \frac{\text{Tr}[\Gamma_{\Delta\mathbb{P}=0}]}{\text{Tr}[\Gamma]} \text{Tr}\left[\Gamma\right]}{\int \{d\mathbf{R}_\alpha\} \int \{d\mathbf{P}_\alpha\}\, e^{-\frac{\beta}{N} H''_{MF}} \text{Tr}\left[\Gamma_{\Delta\mathbb{P}=-1}\right]}. \tag{A.4}$$

Similarly, we rewrite the dynamical recrossing factor as

$$\kappa'_{\text{MF-RPMD}}(t) = \frac{\int \{d\mathbf{R}_\alpha\} \int \{d\mathbf{P}_\alpha\}\, e^{-\frac{\beta}{N} H''_{MF}} \frac{\text{Tr}[\Gamma_{\Delta\mathbb{P}=0}]}{\text{Tr}[\Gamma]} \text{Tr}\left[\Gamma\right] \Delta\dot{\mathbb{P}}_0 h\left(\Delta\mathbb{P}_t\right)}{\int \{d\mathbf{R}_\alpha\} \int \{d\mathbf{P}_\alpha\}\, e^{-\frac{\beta}{N} H''_{MF}} \frac{\text{Tr}[\Gamma_{\Delta\mathbb{P}=0}]}{\text{Tr}[\Gamma]} \text{Tr}\left[\Gamma\right]}. \tag{A.5}$$

Because values of the ratio $\text{Tr}\left[\Gamma_{\Delta\mathbb{P}=0}\right]/\text{Tr}\left[\Gamma\right]$ will be largest near the diabatic crossing point where the physical probability of kinks is highest, we make the

approximation $\mathrm{Tr}\left[\Gamma_{\Delta\mathbb{P}=-1}\right] \approx \mathrm{Tr}\left[\Gamma\right]$ near $\mathbf{R}^{\ddagger}$ and rewrite k'_{TST} and $\kappa'_{\text{MF-RPMD}}(t)$ as follows:

$$k'_{\mathrm{TST}} = \frac{\int \{d\mathbf{R}_\alpha\} \int \{d\mathbf{P}_\alpha\}\, e^{-\frac{\beta}{N} H''_{MF}} \frac{\mathrm{Tr}[\Gamma_{\Delta\mathbb{P}=0}]}{\mathrm{Tr}[\Gamma]} \mathrm{Tr}\left[\Gamma_{\Delta\mathbb{P}=-1}\right]}{\int \{d\mathbf{R}_\alpha\} \int \{d\mathbf{P}_\alpha\}\, e^{-\frac{\beta}{N} H''_{MF}} \mathrm{Tr}\left[\Gamma_{\Delta\mathbb{P}=-1}\right]} \tag{A.6}$$

and

$$\kappa'_{\text{MF-RPMD}}(t) = \frac{\int \{d\mathbf{R}_\alpha\} \int \{d\mathbf{P}_\alpha\}\, e^{-\frac{\beta}{N} H''_{MF}} \frac{\mathrm{Tr}[\Gamma_{\Delta\mathbb{P}=0}]}{\mathrm{Tr}[\Gamma]} \mathrm{Tr}\left[\Gamma_{\Delta\mathbb{P}=-1}\right] \Delta\dot{\mathbb{P}}_0 h\left(\Delta\mathbb{P}_t\right)}{\int \{d\mathbf{R}_\alpha\} \int \{d\mathbf{P}_\alpha\}\, e^{-\frac{\beta}{N} H''_{MF}} \frac{\mathrm{Tr}[\Gamma_{\Delta\mathbb{P}=0}]}{\mathrm{Tr}[\Gamma]} \mathrm{Tr}\left[\Gamma_{\Delta\mathbb{P}=-1}\right]}. \tag{A.7}$$

The ratio $\mathrm{Tr}\left[\Gamma_{\Delta\mathbb{P}=0}\right]/\mathrm{Tr}\left[\Gamma\right]$ in Eqs. (A.6) and (A.7) allows kink formation in a narrow distribution about the diabatic curve intersection point, and the term $\mathrm{Tr}\left[\Gamma_{\Delta\mathbb{P}=-1}\right]$ accounts for the fact that we wish to measure kink probability coming from the reactant state. Monte Carlo sampling to generate an initial distribution for $\kappa'_{\text{MF-RPMD}}$ is best performed on the weighting function

$$W'_1 = e^{-\frac{\beta}{N} H''_{MF}} \frac{\mathrm{Tr}\left[\Gamma_{\Delta\mathbb{P}=0}\right]}{\mathrm{Tr}\left[\Gamma\right]}, \tag{A.8}$$

which limits sampling to the narrow distribution where kink formation is allowed. To calculate k'_{TST}, we propose multiplying and dividing by an additional function, $g(R)$, that allows the solvent ring polymer to easily sample regions near the diabatic crossing as well as in the reactant minimum:

$$k'_{\mathrm{TST}} = \frac{\int \{d\mathbf{R}_\alpha\} \int \{d\mathbf{P}_\alpha\} \left\{e^{-\frac{\beta}{N} H''_{MF}} g(\{\mathbf{R}_\alpha\})\right\} \frac{\mathrm{Tr}[\Gamma_{\Delta\mathbb{P}=0}]}{\mathrm{Tr}[\Gamma]} \frac{\mathrm{Tr}[\Gamma_{\Delta\mathbb{P}=-1}]}{g(\{\mathbf{R}_\alpha\})}}{\int \{d\mathbf{R}_\alpha\} \int \{d\mathbf{P}_\alpha\} \left\{e^{-\frac{\beta}{N} H''_{MF}} g(\{\mathbf{R}_\alpha\})\right\} \frac{\mathrm{Tr}[\Gamma_{\Delta\mathbb{P}=-1}]}{g(\{\mathbf{R}_\alpha\})}}. \tag{A.9}$$

In the equation above, the terms contained in curly brackets are the Monte Carlo weighting functions, and one possible definition of $g(R)$ is

$$g(\{\mathbf{R}_\alpha\}) = \begin{cases} e^{-\alpha_1\left(\overline{\mathbf{R}}-\mathbf{R}^{\ddagger}\right)^2} & \overline{\mathbf{R}} < \mathbf{R}^{\ddagger} \\ e^{-\alpha_2\left(\overline{\mathbf{R}}-\mathbf{R}^{\ddagger}\right)^2} & \overline{\mathbf{R}} > \mathbf{R}^{\ddagger} \end{cases}, \tag{A.10}$$

with $\alpha_1 > \alpha_2$ in the inverted regime.

Preliminary tests suggest the scheme above properly allows for tunneling by loosening the constraint on kink formation to a small distribution about the diabatic crossing. However, we find that the current definition of $\Delta\mathbb{P}$ used to calculate the recrossing factor fails for initial configurations except where $\overline{\mathbf{R}} = \mathbf{R}^{\ddagger}$. This is most likely because $\Delta\mathbb{P}$ is dominated by terms involving the lowest energy state, and unless $\overline{\mathbf{R}} = \mathbf{R}^{\ddagger}$ it cannot properly recognize a change in electronic state populations between $t = 0$ and later times. An improved definition of $\Delta\mathbb{P}$ for calculating the initial velocity is needed before this scheme can be used. If one does not exist in the mean field framework, we may need to use a method like MV-RPMD, since it employs explicit variables for the electronic states and should, in theory, recognize initial changes in populations.

APPENDIX B

THE SINGLE-BEAD LIMIT IN MAPPING VARIABLE RING POLYMER MOLECULAR DYNAMICS

With so few beads required to converge the simulations presented in Chapter 4 ($N < 9$), one wonders how MV-RPMD performs in the single-bead limit ($N = 1$) for these model systems—here we provide those results [7]. Populations as a function of time for Models I-III are shown in Fig. B.1, results for Models IV-VI are provided in Fig. B.2, and the number of trajectories required to converge the populations to second decimal place, along with the timesteps needed to conserve energy, are provided in Table B.1.

The single bead case represents the classical limit of nuclear dynamics but corresponds to the $\beta\Delta \ll 1$ limit for the electronic degrees of freedom. Since both conditions are satisfied in the three photodissociation models, it is not surprising that the single-bead limit performs exceptionally well for these systems. Although these results are unconverged in bead number and are, therefore, not fully reliable, the single bead limit performs well enough for the three-state models to suggest that it may provide significant insight into the dynamics of other photochemical systems for which the nuclei are nearly classical.[1]

[1]One could argue that the $N = 1$ limit out-performs the bead-converged simulations; it is possible that some of the internal ring polymer frequencies for $N > 1$ make the dynamics less accurate. We will investigate this idea further in future studies.

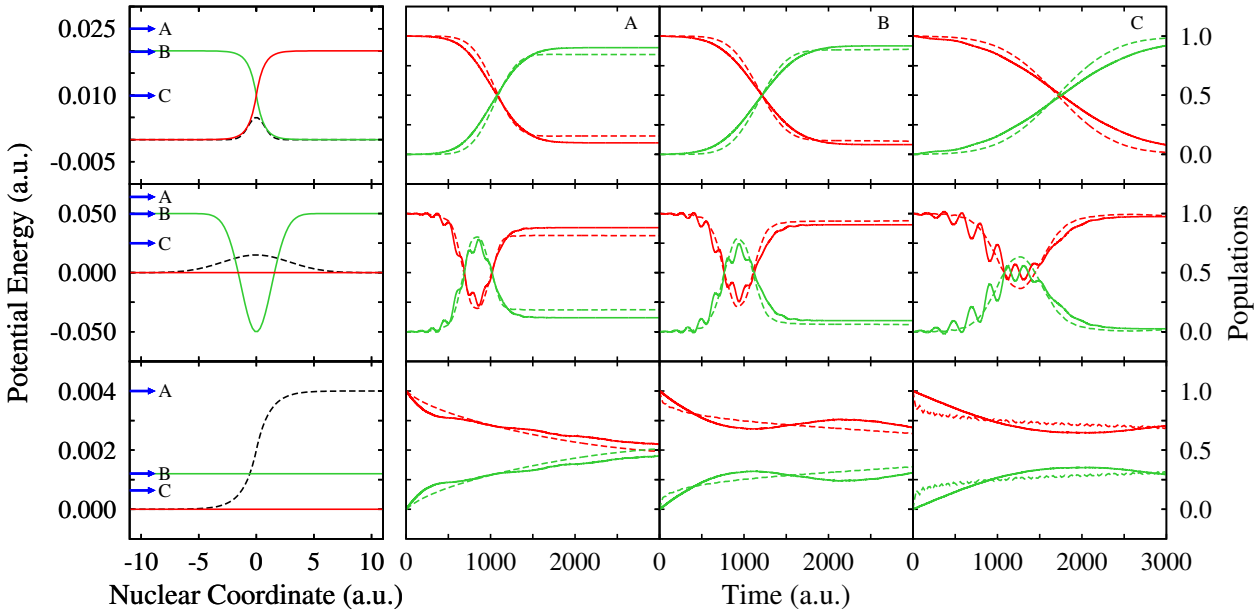

Figure B.1: Diabatic potential energy functions and real-time electronic state populations using $N = 1$ for Models I, II, and III (top, middle, and bottom rows, respectively) described in Section 4.4.1. The first column shows potential curves with solid colored lines and coupling functions with black dashed lines (the coupling function for Model III is scaled by 0.02 for clarity). Kinetic energies associated with the three values of P_0 tested for each model are indicated with blue arrows and are labeled to correspond to results in panels A, B, and C. MV-RPMD results in each panel are shown with solid lines, exact quantum results are shown with dashed lines, and lines are colored to match the diabats in the first column.

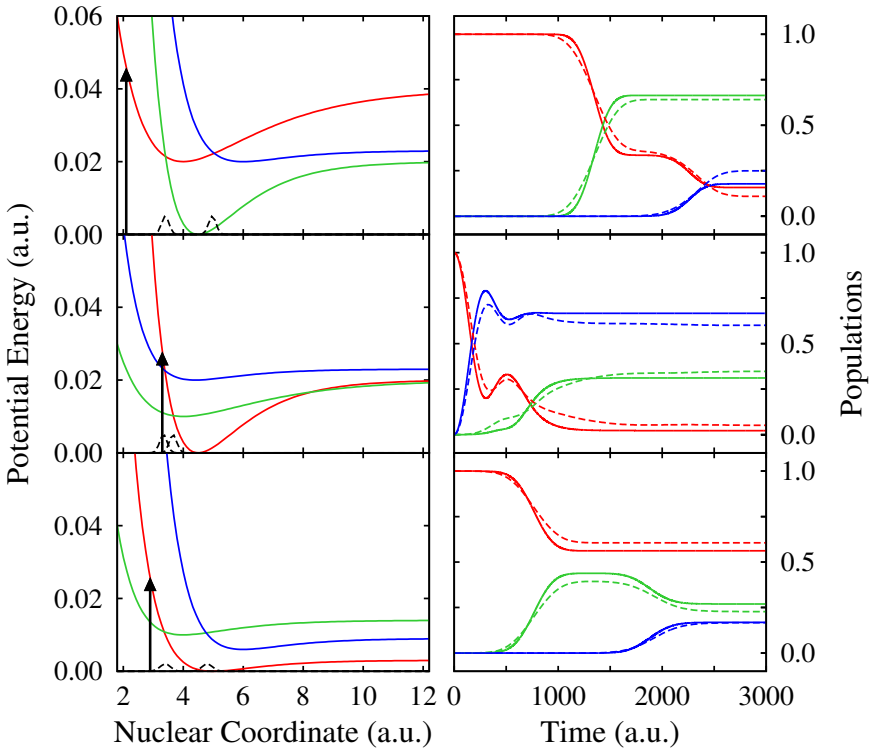

Figure B.2: Diabatic potential energy curves and real-time electronic state populations using $N = 1$ for Models IV, V, and VI (top, middle, and bottom rows, respectively) described in Section 4.5.1. The left column shows potential curves with solid lines and coupling functions with dashed lines; the center of the initial nuclear wavefunction constrained to excited state 1 is indicated by a black arrow. The right column shows MV-RPMD results with solid lines and exact quantum results with dashed lines; lines are colored to match the diabats in the left column.

Table B.1: The number of trajectories and timesteps used in the MV-RPMD simulations for the two- and three-state models described in Sections 4.4.1 and 4.5.1 in the single-bead limit. The two-state models are labeled by P_0, the center of the initial forward momentum distribution of the wavepacket, which is reported in atomic units.

Model	P_0	Trajectories	dt
I	6.3	7200	0.1
	8.9	2400	0.1
	10	1920	0.1
II	10	4800	0.1
	14.1	4800	0.1
	16	2880	0.1
III	1.6	3600	0.005
	2.2	5280	0.005
	4	9600	0.005
IV	–	1200	0.1
V	–	4500	0.1
VI	–	1800	0.1

BIBLIOGRAPHY

[1] David Chandler and Peter G. Wolynes. Exploiting the isomorphism between quantum theory and classical statistical mechanics of polyatomic fluids. *J. Chem. Phys.*, 74:4078–4095, 1981.

[2] Ian R. Craig and David E. Manolopoulos. Quantum statistics and classical mechanics: Real time correlation functions from ring polymer molecular dynamics. *J. Chem. Phys.*, 121:3368–3373, 2004.

[3] Scott Habershon, David E. Manolopoulos, Thomas E. Markland, and Thomas F. Miller, III. Ring-polymer molecular dynamics: Quantum effects in chemical dynamics from classical trajectories in an extended phase space. *Annu. Rev. Phys. Chem.*, 64:387–413, 2013.

[4] The mean field RPMD approximation is not a new idea and has been used previously to benchmark nonadiabatic path integral methods by D. E. Manolopoulos, T. F. Miller III, N. Ananth, J. C. Tully, and I. R. Craig. See, for instance, "An electronically non-adiabatic generalization of ring polymer molecular dynamics," T. J. H. Hele, MChem thesis, Exeter College, University of Oxford, 2011.

[5] Jessica R. Duke and Nandini Ananth. Mean field ring polymer molecular dynamics for electronically nonadiabatic reaction rates. *Farad. Discuss.*, 195:253–268, 2016.

[6] Nandini Ananth. Mapping variable ring polymer molecular dynamics: A path-integral based method for nonadiabatic processes. *J. Chem. Phys.*, 139:124102, 2013.

[7] Jessica R. Duke and Nandini Ananth. Simulating excited state dynamics in systems with multiple avoided crossings using mapping variable ring polymer molecular dynamics. *J. Phys. Chem. Lett.*, 6(21):4219–4223, 2015.

[8] Marshall D. Newton and Norman Sutin. Electron transfer reactions in condensed phases. *Annu. Rev. Chem.*, 35:437–480, 1984.

[9] Harry B. Gray and Jay R. Winkler. Electron transfer in proteins. *Annu. Rev. Biochem.*, 65:537–561, 1996.

[10] Robert I. Cukier and Daniel G. Nocera. Proton-coupled electron transfer. *Annu. Rev. Phys. Chem.*, 49:337–369, 1998.

[11] Michael Grätzel. Photoelectrochemical cells. *Nature*, 414:338–344, 2001.

[12] Michael Grätzel. Dye-sensitized solar cells. *J. Photochem. Photobiol. C*, 4:145–153, 2003.

[13] Nathan S. Lewis and Daniel G. Nocera. Powering the planet: Chemical challenges in solar energy utilization. *Proc. Natl. Acad. Sci. U.S.A.*, 103:15729–15735, 2006.

[14] My Hang V. Huynh and Thomas J. Meyer. Proton-coupled electron transfer. *Chem. Rev.*, 107:5004–5064, 2007.

[15] Bernard Kippelen and Jean-Luc Brédas. Organic photovoltaics. *Energy Environ. Sci.*, 2:251–261, 2009.

[16] S. Y. Reece and D. G. Nocera. Proton-coupled electron transfer in biology: Results from synergistic studies in natural and model systems. *Annu. Rev. Biochem.*, 78:673–699, 2009.

[17] Yasuhiro Tachibana, Lionel Vayssieres, and James R. Durrant. Artificial photosynthesis for solar water-splitting. *Nat. Photon.*, 6:511–518, 2012.

[18] Nancy Makri. Time-dependent quantum methods for large systems. *Annu. Rev. Phys. Chem.*, 50:167–191, 1999.

[19] John C. Tully. Molecular dynamics with electronic transitions. *J. Chem. Phys.*, 93:1061–1071, 1990.

[20] Jianshu Cao and Gregory A. Voth. The formulation of quantum statistical mechanics based on the Feynman path centroid density. I. Equilibrium properties. *J. Chem. Phys.*, 100:5093–5105, 1994.

[21] Xiong Sun, Haobin Wang, and William H. Miller. Semiclassical theory of electronically nonadiabatic dynamics: Results of a linearized approximation to the initial value representation. *J. Chem. Phys.*, 109:7064–7074, 1998.

[22] Michael Thoss and Haobin Wang. Semiclassical description of molecular dynamics based on initial-value representation methods. *Annu. Rev. Phys. Chem.*, 55:299–332, 2004.

[23] Raymond Kapral. Progress in the theory of mixed quantum-classical dynamics. *Annu. Rev. Phys. Chem.*, 57:129–157, 2006.

[24] Nandini Ananth, Charulatha Venkataraman, and William H. Miller. Semiclassical description of electronically nonadiabatic dynamics via the initial value representation. *J. Chem. Phys.*, 127:084114, 2007.

[25] Stephen J. Cotton and William H. Miller. Symmetrical windowing for quantum states in quasi-classical trajectory simulations. *J. Phys. Chem. A*, 117:7190–7194, 2013.

[26] Jeremy O. Richardson and Michael Thoss. Communication: Nonadiabatic ring-polymer molecular dynamics. *J. Chem. Phys.*, 139:031102, 2013.

[27] Artur R. Menzeleev, Franziska Bell, and Thomas F. Miller, III. Kinetically constrained ring-polymer molecular dynamics for non-adiabatic chemical reactions. *J. Chem. Phys.*, 140:064103, 2014.

[28] Jian Liu. Recent advances in the linearized semiclassical initial value representation/classical Wigner model for the thermal correlation function. *Int. J. Quantum Chem.*, 115:657–670, 2015.

[29] M. K. Lee, P. Huo, and David F. Coker. Semiclassical path integral dynamics: Photosynthetic energy transfer with realistic environment interactions. *Annu. Rev. Phys. Chem.*, 67:27.1–27.31, 2016.

[30] Joseph E. Subotnik, Amber Jain, Brian Landry, Andrew Petit, Wenjun Ouyang, and Nicole Bellonzi. Understanding the surface hopping view of electronic transitions and decoherence. *Annu. Rev. Phys. Chem.*, 67:387–417, 2016.

[31] Thomas F. Miller, III and David E. Manolopoulos. Quantum diffusion in liquid para-hydrogen from ring-polymer molecular dynamics. *J. Chem. Phys.*, 122:184503, 2005.

[32] Nicholas Boekelheide, Romelia Salomón-Ferrer, and Thomas F. Miller, III. Dynamics and dissipation in enzyme catalysis. *Proc. Natl. Acad. Sci. U.S.A.*, 108:16159–16163, 2011.

[33] Rachel L. Kenion and Nandini Ananth. Direct simulation of electron transfer in the cobalt hexammine(II/III) self-exchange reaction. *Phys. Chem. Chem. Phys.*, 18:26117–26124, 2016.

[34] Ian R. Craig and David E. Manolopoulos. Chemical reaction rates from ring polymer molecular dynamics. *J. Chem. Phys.*, 122:084106, 2005.

[35] Ian R. Craig and David E. Manolopoulos. A refined ring polymer molecular dynamics theory of chemical reaction rates. *J. Chem. Phys.*, 123:034102, 2005.

[36] Thomas F. Miller, III and David E. Manolopoulos. Quantum diffusion in liquid water from ring polymer molecular dynamics. *J. Chem. Phys.*, 123:154504, 2005.

[37] Rosana Collepardo-Guevara, Ian R. Craig, and David E. Manolopoulos. Proton transfer in a polar solvent from ring polymer reaction rate theory. *J. Chem. Phys.*, 128:144502, 2008.

[38] Thomas F. Miller, III. Isomorphic classical molecular dynamics model for an excess electron in a supercritical fluid. *J. Chem. Phys.*, 129:194502, 2008.

[39] Thomas E. Markland, Scott Habershon, and David E. Manolopoulos. Quantum diffusion of hydrogen and muonium atoms in liquid water and hexagonal ice. *J. Chem. Phys.*, 128:194506, 2008.

[40] Scott Habershon, Thomas E. Markland, and David E. Manolopoulos. Competing quantum effects in the dynamics of a flexible water model. *J. Chem. Phys.*, 131:024501, 2009.

[41] Thomas E. Markland, Joseph A. Morrone, Bruce J. Berne, Kunimasa Miyazaki, Eran Rabani, and David R. Reichman. Quantum fluctuations can promote or inhibit glass formation. *Nat. Phys.*, 137:134–137, 2011.

[42] Artur R. Menzeleev, Nandini Ananth, and Thomas F. Miller, III. Direct simulation of electron transfer using ring polymer molecular dynamics: Com-

parison with semiclassical instanton theory and exact quantum methods. *J. Chem. Phys.*, 135:074106, 2011.

[43] Yury V. Suleimanov, Rosana Collepardo-Guevara, and David E. Manolopoulos. Bimolecular reaction rates from ring polymer molecular dynamics: Application to $H + CH_4 \rightarrow H_2 + CH_3$. *J. Chem. Phys.*, 134:044131, 2011.

[44] Yury V. Suleimanov. Surface diffusion of hydrogen on Ni(100) from ring polymer molecular dynamics. *J. Chem. Phys.*, 116:11141–11153, 2012.

[45] David M. Wilkins, David E. Manolopoulos, and Liem X. Dang. Nuclear quantum effects in water exchange around lithium and fluoride ions. *J. Chem. Phys.*, 142:064509, 2015.

[46] Piotr Kowalczyk, Artur P. Terzyk, Piotr A. Gauden, Sylwester Furmaniak, Katsumi Kaneko, and Thomas F. Miller, III. Nuclear quantum effects in the layering and diffusion of hydrogen isotopes in carbon nanotubes. *J. Phys. Chem. Lett.*, 6:3367–3372, 2015.

[47] Joshua S. Kretchmer and Thomas F. Miller, III. Kinetically-constrained ring-polymer molecular dynamics for non-adiabatic chemistries involving solvent and donor-acceptor dynamical effects. *Farad. Discuss.*, 195:191–214, 2016.

[48] H. F. Trotter. On the product of semi-groups of operators. *Proc. Amer. Math. Soc.*, 10:545–551, 1959.

[49] Ryan P. Steele, Jill Zwickl, Philip Shushkov, and John C. Tully. Mixed time slicing in path integral simulations. *J. Chem. Phys.*, 134:074112, 2011.

[50] Michele Parrinello and Aneesur Rahman. Study of an F center in molten KCl. *J. Chem. Phys.*, 80:860–867, 1984.

[51] Richard P. Feynman and Albert R. Hibbs. *Quantum Mechanics and Path Integrals*. McGraw-Hill, New York, 1965.

[52] J. A. Barker. A quantum-statistical Monte Carlo method; path integrals with boundary conditions. *J. Chem. Phys.*, 70:2914–2918, 1979.

[53] Ryogo Kubo. Statistical-mechanical theory of irreversible processes. I. General theory and simple applications to magnetic and conduction problems. *J. Phys. Soc. Jpn.*, 12:570–586, 1957.

[54] Lawrence S. Schulman. *Techniques and Applications of Path Integration*. John Wiley and Sons, Inc., New York, 1981.

[55] Nancy Makri. Numerical path integral techniques for long time dynamics of quantum dissipative systems. *J. Math. Phys.*, 36:2430–2457, 1995.

[56] Timothy J. H. Hele, Michael J. Willatt, Andrea Muolo, and Stuart C. Althorpe. Boltzmann-conserving classical dynamics in quantum time-correlation functions: "Matsubara dynamics". *J. Chem. Phys.*, 142:134103, 2015.

[57] Timothy J. H. Hele, Michael J. Willatt, Andrea Muolo, and Stuart C. Althorpe. Communication: Relation of centroid molecular dynamics and ring-polymer molecular dynamics to exact quantum dynamics. *J. Chem. Phys.*, 142:191101, 2015.

[58] Timothy J. H. Hele and Stuart C. Althorpe. Derivation of a true ($t \to 0^+$) quantum transition-state theory. I. Uniqueness and equivalence to

ring-polymer molecular dynamics transition-state-theory. *J. Chem. Phys.*, 138:084108, 2013.

[59] Stuart C. Althorpe and Timothy J. H. Hele. Derivation of a true ($t \to 0^+$) quantum transition-state theory. II. Recovery of the exact quantum rate in the absence of recrossing. *J. Chem. Phys.*, 139:084115, 2013.

[60] Ralph Welsch, Kai Song, Qiang Shi, Stuart C. Althorpe, and Thomas F. Miller, III. Non-equilibrium dynamics from RPMD and CMD. *J. Chem. Phys.*, 145:204118, 2016.

[61] William H. Miller, Steven D. Schwartz, and John W. Tromp. Quantum mechanical rate constants for bimolecular reactions. *J. Chem. Phys.*, 79:4889–4898, 1983.

[62] David Chandler. *Introduction to Modern Statistical Mechanics*. Oxford University Press, New York, 1987.

[63] Daan Frenkel and Berend Smit. *Understanding Molecular Simulation*. Academic Press, California, 2 edition, 2002.

[64] G. M. Torrie and J. P. Valleau. Nonphysical sampling distributions in Monte Carlo free-energy estimation: Umbrella sampling. *J. Comput. Phys.*, 23:187–199, 1977.

[65] Shankar Kumar, John M. Rosenberg, Djamal Bouzida, Robert H. Swendsen, and Peter A. Kollman. The weighted histogram analysis method for free-energy calculations on biomolecules. I. The method. *J. Comput. Chem.*, 13:1011–1021, 1992.

[66] Maria Topaler and Nancy Makri. Quantum rates for a double well coupled

to a dissipative bath: Accurate path integral results and comparison with approximate theories. *J. Chem. Phys.*, 101:7500–7519, 1994.

[67] E. Fermi. *Nuclear Physics*. University of Chicago Press, 1950.

[68] Jens Ulstrup and Joshua Jortner. The effect of intramolecular quantum modes on free energy relationships for electron transfer reactions. *J. Chem. Phys.*, 63:4358–4368, 1975.

[69] Jens Ulstrup. *Charge Transfer Processes in Condensed Media*. Springer Verlag, Berlin, 1979.

[70] Niels E. Henriksen and Flemming Y. Hansen. *Theories of Molecular Reaction Dynamics*. Oxford University Press, New York, 2008.

[71] Nancy Makri. Stabilization of localized states in dissipative tunneling systems interacting with monochromatic fields. *J. Chem. Phys.*, 106:2286–2297, 1996.

[72] R. A. Marcus and Norman Sutin. Electron transfers in chemistry and biology. *Biochim. Biophys. Acta*, 811:265–322, 1985.

[73] Hans-Dieter Meyer and William H. Miller. A classical analog for electronic degrees of freedom in nonadiabatic collision processes. *J. Chem. Phys.*, 70:3214–3223, 1979.

[74] Gerhard Stock and Michael Thoss. Semiclassical description of nonadiabatic quantum dynamics. *Phys. Rev. Lett.*, 78:578–581, 1979.

[75] Nandini Ananth and Thomas F. Miller, III. Exact quantum statistics for electronically nonadiabatic systems using continuous path variables. *J. Chem. Phys.*, 133:234103, 2010.

[76] William B. Case. Wigner functions and Weyl transforms for pedestrians. *Am. J. Phys.*, 76:937–946, 2008.

[77] Timothy J. H. Hele and Nandini Ananth. Deriving the exact nonadiabatic quantum propagator in the mapping variable representation. *Farad. Discuss.*, 195:269–289, 2016.

[78] Sara Bonella and David F. Coker. Semiclassical implementation of the mapping hamiltonian approach for nonadiabatic dynamics using focused initial distribution sampling. *J. Chem. Phys.*, 118:4370–4385, 2003.

[79] Daniel T. Colbert and William H. Miller. A novel discrete variable representation for quantum mechanical reactive scattering via the S- matrix Kohn method. *J. Chem. Phys.*, 96:1982–1991, 1992.

[80] Neil Shenvi, Joseph E. Subotnik, and Weitao Yang. Simultaneous-trajectory surface hopping: A parameter-free algorithm for implementing decoherence in nonadiabatic dynamics. *J. Chem. Phys.*, 134:144102, 2011.

[81] Eduardo A. Coronado, Jianhua Xing, and William H. Miller. Ultrafast nonadiabatic dynamics of systems with multiple surface crossings: A test of the Meyer-Miller hamiltonian with semiclassical initial value representation methods. *Chem. Phys. Lett.*, 349:521–529, 2001.

[82] Austin T. Green, Jessica R. Duke, and Nandini Ananth. Reaction rates from mean field ring polymer molecular dynamics in the strong friction regime. *Manuscript in preparation*.

[83] Sadrach Pierre, Jessica R. Duke, Timothy J. H. Hele, and Nandini Ananth. Investigating the mechanisms of proton-coupled electron transfer: A map-

ping variable ring polymer molecular dynamics study. *Manuscript in preparation*.